

Stabilization of a Complex Perovskite Superstructure under Ambient Conditions: Influence of Cation Composition and Ordering, and Evaluation as an SOFC Cathode

A. Demont,[†] M. S. Dyer,[†] R. Sayers,[†] M. F. Thomas,[‡] M. Tsiamtsouri,[†] H. N. Niu,[†] G. R. Darling,[†] A. Daoud-Aladine,[§] J. B. Claridge,[‡] and M. J. Rosseinsky*,[†]

[†]Department of Chemistry, University of Liverpool, Liverpool L69 7ZD, United Kingdom, [‡]Department of Physics, University of Liverpool, Liverpool L69 7ZE, United Kingdom, and [§]ISIS Facility, Rutherford Appleton Laboratory, Chilton, Didcot, Oxfordshire OX11 0QX, United Kingdom

Received August 29, 2010. Revised Manuscript Received October 9, 2010

$\text{Ba}_{1.6}\text{Ca}_{2.3}\text{Y}_{1.1}\text{Fe}_{5}\text{O}_{13}$ is an Fe^{3+} oxide adopting a complex perovskite superstructure, which is an ordered intergrowth between the $\text{Ca}_2\text{Fe}_2\text{O}_5$ and $\text{YBa}_2\text{Fe}_3\text{O}_8$ structures featuring octahedral, square pyramidal, and tetrahedral B sites and three distinct A site environments. The distribution of A site cations was evaluated by combined neutron and X-ray powder diffraction. Consistent with the Fe^{3+} charge state, the material is an antiferromagnetic insulator with a Néel temperature of 480–485 °C and has a relatively low d.c. conductivity of 2.06 S cm⁻¹ at 700 °C. The observed area specific resistance in symmetrical cell cathodes with the samarium-doped ceria electrolyte is 0.87 Ω cm² at 700 °C, consistent with the square pyramidal Fe^{3+} layer favoring oxide ion formation and mobility in the oxygen reduction reaction. Density functional theory calculations reveal factors favoring the observed cation ordering and its influence on the electronic structure, in particular the frontier occupied and unoccupied electronic states.

Introduction

Transition metal oxides are of importance due to the wide array of functional behavior they display.^{1–4} Among these compounds, the ABO_3 perovskite has a pronounced structural flexibility that allows considerable compositional diversity, resulting in a rich array of accessible and chemically tunable properties.⁵ A site cation and oxygen vacancy ordering are directly linked to the transition metal environment and oxidation state, and have a dramatic influence on the targeted behavior of the compounds.^{6–8} Control of these features can therefore be of crucial importance for the generation of interesting new properties. One important application area is in solid

oxide fuel cell (SOFC) cathodes^{9–13} – in an SOFC, the cathode is responsible for the catalysis of the reduction of the dioxygen O_2 molecule to O^{2-} and must be a mixed electronic conductor (to deliver electrons liberated from the fuel at the anode to reduce O_2) and ionic conductor (to transport the generated oxide ions via the electrolyte to the anode for fuel oxidation) stable in an oxidizing atmosphere. Transition metal oxides are thus the appropriate materials class for this application. The recent identification of specific structural features such as the oxygen vacancy layers in $\text{NdBaCo}_2\text{O}_{5+x}$ ^{6–8} as being responsible for enhancing cathode properties (in this case by increased oxide ion mobility) offers the opportunity of enhanced cathode performance in materials where the structure allows the optimization of all three required functions. Recent reviews of SOFC cathode materials^{14,15} treat this problem in more detail. In brief, the leading cathode candidates are $\text{ABO}_{3-\delta}$ perovskite-related materials such as Co-rich BSCF ($\text{Ba}_{0.5}\text{Sr}_{0.5}\text{Co}_{0.8}\text{Fe}_{0.2}\text{O}_{3-\delta}$)¹ and Fe-rich LSCF ($\text{La}_{0.6}\text{Sr}_{0.4}\text{Fe}_{0.8}\text{Co}_{0.2}\text{O}_{3-\delta}$)¹⁶ where oxygen vacancies generate the ionic conduction, but the combined challenges of minimizing electrode polarization resistance through optimizing the three functions

*Corresponding author. E-mail: m.j.rosseinsky@liverpool.ac.uk.
(1) Shao, Z.; Haile, S. M. *Nature* **2004**, *431*, 170–173.
(2) Dawber, M.; Rabe, K.; Scott, J. *Rev. Mod. Phys.* **2005**, *77*, 1083–1130.
(3) Kim, C. H.; Qi, G.; Dahlberg, K.; Li, W. *Science* **2010**, *327*, 1624.
(4) Pena, M.; Fierro, J. *Chem. Rev.* **2001**, *101*, 1981–2017.
(5) Mitchell, R. H., *Perovskites Modern and Ancient*; Almaz Press: Thunder Bay, Ontario, 2002.
(6) Taskin, A. A.; Lavrov, A. N.; Ando, Y. *Appl. Phys. Lett.* **2005**, *86*, 091910.
(7) Taskin, A. A.; Lavrov, A. N.; Ando, Y. *Prog. Solid State Chem.* **2007**, *35*, 481–490.
(8) Kim, G.; Wang, S.; Jacobson, A. J.; Yuan, Z.; Donner, W.; Chen, C. L.; Reimus, C.; Brodersen, P.; Mims, C. A. *Appl. Phys. Lett.* **2006**, *88*, 024103.
(9) Tarancón, A.; Burriel, M.; Santiso, J.; Skinner, S. J.; Kilner, J. A. *J. Mater. Chem.* **2010**, *20*, 3799–3813.
(10) Kilner, J. A.; Irvine, J. T. S. *Handbook of Fuel Cells*; Wiley: New York, 2009; Vol. 5, pp 489–504.
(11) Hou, S.; Alonso, J. A.; Rajasekhara, S.; Martínez-Lope, M. J.; Fernández-Díaz, M. T.; Goodenough, John B. *Chem. Mater.* **2010**, *22*, 1071–1079.
(12) Nicholas, J. D.; Barnett, S. A. *J. Electrochem. Soc.* **2010**, *157*, 536–541.
(13) Aksanova, T. V.; Gavrilova, L. Y.; Yaremchenko, A. A.; Cherepanov, V. A.; Kharton, V. V. *Mater. Res. Bull.* **2010**, *45*, 1288–1292.
(14) Jacobson, A. J. *Chem. Mater.* **2010**, *22*, 660–674.
(15) Orera, A.; Slater, P. R. *Chem. Mater.* **2010**, *22*, 675–690.
(16) Bae, J.-M.; Steele, B. C. H. *Solid State Ionics* **1998**, *106*, 247–253.

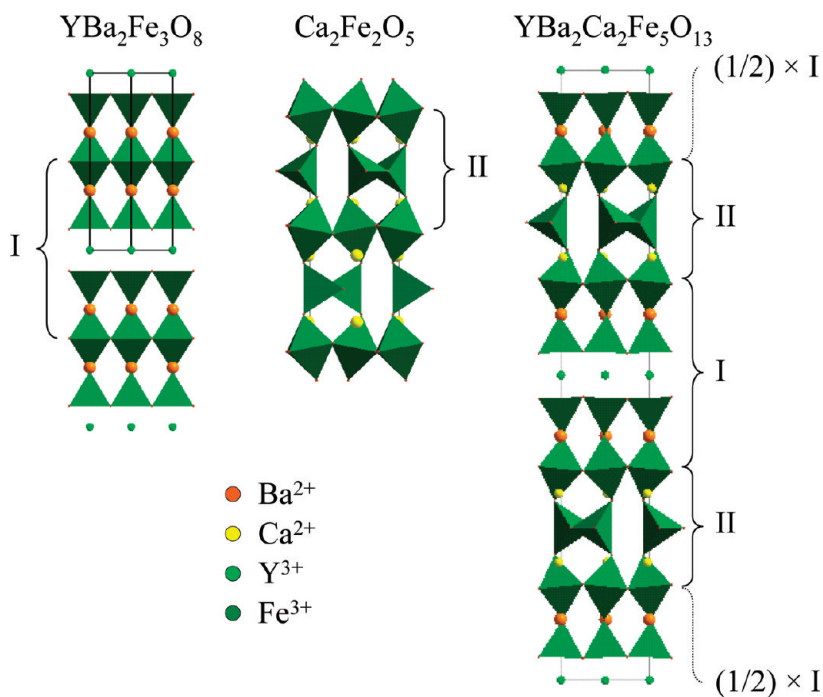


Figure 1. Structures of $\text{YBa}_2\text{Fe}_3\text{O}_8$, $\text{Ca}_2\text{Fe}_2\text{O}_5$, and the ideal 10-layer intergrowth $\text{YBa}_2\text{Ca}_2\text{Fe}_5\text{O}_{13}$. Building units I and II (marked by brackets) of the two former structures are regularly stacked in a 1:1 ratio to form the ideal $\text{YBa}_2\text{Ca}_2\text{Fe}_5\text{O}_{13}$.

listed above whilst avoiding reactivity with the electrolyte and matching thermal expansion with other components of the fuel cell make the identification of a suitable cathodes for the intermediate temperature range (500–700 °C) one of the key tasks for the development of this technology.

One way to address this challenge is to investigate candidate cathodes with distinct domains within their structures – these distinct regions could in principle allow optimization of each of the required functions. The perovskite structure has a very rich ordered defect chemistry leading to complex superstructures with multiple transition metal and A cation environments.¹⁷ Recently, Tenailleau *et al.* reported $\text{Ba}_2\text{Ca}_2\text{Nd}_2\text{Fe}_6\text{O}_{15.6}$ with a perovskite superstructure of high structural complexity, featuring three distinct environments for both A and B site cations,¹⁸ offering new perspectives in the interplay between A site order, oxygen content and transition metal oxidation state and environment. The A site order leads to the anion vacancy ordering and resulting multiple transition metal coordination environments. The structure, consisting of 10 repeat layers in the stacking direction, is thus an interesting one to consider from the point of view of SOFC cathodes, but the first example has an iron oxidation state of less than 3 and is therefore unsuitable for application in the SOFC cathode environment (> 500 °C, air). Here we report a new isostructural Fe^{3+} material by control of the A site composition to stabilize this ten layer superstructure under ambient oxygen pressure conditions over a wide temperature range. The material is structurally a 1:1

intergrowth of the Fe^{3+} compounds $\text{Ca}_2\text{Fe}_2\text{O}_5$ ¹⁹ and $\text{YBa}_2\text{Fe}_3\text{O}_8$ ²⁰ (Figure 1). The resulting air stability at high temperature allows evaluation of the SOFC cathode behavior of the material which is surprisingly good given the high dc resistance produced by the integer charge Fe^{3+} composition. The electronic properties are dominated by the Fe^{3+} oxidation state as confirmed by Mössbauer spectroscopy and leading to G-type antiferromagnetic ordering.

We have used DFT calculations to investigate the effect of the multiple A and B site environments on the electronic structure and stability of the compound. Using supercell calculations to model partial occupancy at the crystallographic A sites, we show that the occupation of A sites with different cations has a large effect on the energy levels of the Fe 3d states centered on the B sites, and consequently on the energy and character of the frontier electronic states at the top of the valence band and bottom of the conduction band. These results have potential implications for the material's electronic conductivity, catalytic activity, and stability.

Experimental Section

Polycrystalline samples were prepared by direct reaction of Y_2O_3 (Alfa Aesar, 99.99%), BaCO_3 (Alfa Aesar, 99.997%), CaCO_3 (Alfa Aesar, 99.99%), and Fe_2O_3 (Alfa Aesar, 99.998%) at 1200 °C in alumina crucibles under ambient air atmosphere, with cationic ratios listed in the Supporting Information (Table SII). The starting materials were previously dried at 180 °C, except Y_2O_3 , which was held at 900 °C before being weighed, to avoid $\text{Y}(\text{OH})_3$ contamination by moisture uptake. The synthesis

(17) Anderson, M. T.; Greenwood, K. B.; Taylor, G. A.; Poepelmeier, K. R. *Prog. Solid State Chem.* **1993**, *22*, 197–233.

(18) Tenailleau, C.; Alix, M.; Claridge, J. B.; Hervieu, M.; Thomas, M. F.; Hirst, J. P.; Rosseinsky, M. J. *J. Am. Chem. Soc.* **2008**, *440*, 7570–7583.

(19) Bertaut, E. F.; Blum, P.; Sagnieres, A. *Acta Crystallogr., Sect. B* **1959**, *12*, 149–159.

(20) Huang, Q.; Karen, P.; Karen, V. L.; Kjekshus, A.; Lynn, J. W.; Michell, A. D.; Rosov, N.; Santoro, A. *Phys. Rev. B* **1992**, *45*, 9611–9619.

heating and cooling rates were respectively 5 and 3°/mn, whereas the heating time was 12 h. Several cycles of regrinding and firing were generally performed to ensure phase homogeneity and complete the reaction process. With the appropriate metal ratios described in the Results section, three of these cycles could reproducibly produce a 5 g single-phase sample. Phase identification and purity were examined by powder X-ray diffraction (PXD) collected on a Panalytical system using Co K α_1 radiation in Bragg–Brentano geometry. Thermogravimetric analysis (TGA) was performed using a TA Instruments Q600 thermal analyzer. Cationic composition was estimated by energy-dispersive X-ray spectroscopy (EDS), performed on a JEOL 2000FX transmission electron microscope.

Crystal structure analysis was carried out on both powder X-ray diffraction and powder neutron diffraction. The X-ray experiment was carried out at station I11 of the Diamond Light Source over a 2 θ range of 2.836 to 141.970° ($\lambda = 0.82678$ Å). Data were collected at room temperature and from 100 to 900 °C in steps of 100 °C. High resolution neutron powder diffraction data were collected on the HRPD beamline at ISIS Rutherford Appleton laboratory. Data were initially collected for 3 h at room temperature then 5 min scans were performed at 450, 475, 480, and 485 °C. At the latter temperature, magnetic ordering peaks were not observed, and data were collected for a further 3 h. Structural parameters were refined by the Rietveld method using the software FULLPROF included in the WINPLOTR package.²¹ Bond valence sums (B.V.S.) were calculated according to Brown and Altermatt.²²

⁵⁷Fe Mössbauer spectra were recorded at 77 and 298 K with a constant acceleration spectrometer. Chemical isomer shifts are relative to metallic iron at room temperature.

DC conductivity data were collected by the standard four-probe method on a bar with approximate dimensions of 2 × 2 × 10 mm³. Pt paste was used to bond the Pt wires in a four-in-a-line contact geometry. In order to limit the grain boundary contribution to the measurement, the material was processed to obtain a dense object. An as-made Ba_{1.7}Ca_{2.3}Y_{1.1}Fe₅O₁₃ single-phase sample was introduced into a FRITSCH Pulverizette 7 classic instrument and ball-milled for 48 h in ethanol media. The resulting fine powder was mixed with a 2% polyvinyl alcohol (PVA) solution in water before being dried overnight. The PVA mass fraction was adjusted to 3% of the total sample mass. The sample was then pressed into a pellet via cold-isostatic pressing (CIP) at 200 MPa and the final step of the synthesis was then repeated with an extended heating time of 24 h at 1200 °C. Pellets obtained by this procedure were of a theoretical density >90%. Phase purity was checked before and after the d.c. conductivity measurement by PXD.

Chemical compatibility tests between the cathode and the electrolytes samarium doped ceria (SDC, Ce_{0.8}Sm_{0.2}O₂) and Yttrium stabilized Zirconia (YSZ, 8 mol % Y₂O₃-doped ZrO₂) were carried out. The material and electrolyte were mixed with a weight ratio of 1:1, pressed into pellets and fired at 1150 °C for 12 h before analyzing the resulting sample by PXD. A symmetrical cell composed of Ba_{1.6}Ca_{2.3}Y_{1.1}Fe₅O₁₃/SDC/Ba_{1.6}Ca_{2.3}Y_{1.1}Fe₅O₁₃ was formulated. Dense (>98% theoretical density), single-phase pellets of SDC were obtained by uniaxial and

isopressing commercial (Fuel Cell Materials) powder into green pellets, followed by sintering at 1400 °C for 5 h. The SDC surface was polished with SiC paper to obtain a flat surface prior to screen printing with the cathode ink. The ink was formulated from Ba_{1.6}Ca_{2.3}Y_{1.1}Fe₅O₁₃ powder mixed by ball-milling with an organic binder (Heraeus V006), which was screen printed onto both surfaces of the SDC electrolyte. Adherence of the ink to the SDC surface was achieved after calcining at 1150 °C for 3 h in air. Gold gauze fixed with gold paste was used as current collection for the electrical measurement. AC impedance spectroscopy was performed on the symmetrical cell over a frequency range of 1 MHz to 0.1 Hz using a Solartron 1260 FRA with a modulation potential of 10 mV, over the temperature range of 873–1073 K in static air. Measurements were made using ZPlot v.2.9b (Scribner Associates) and equivalent circuit modeling was performed using ZView v.2.8 (Scribner Associates). The area specific resistance (ASR) of the cathode was calculated by normalizing the measured resistance for the electrode area and dividing by two to take into account the symmetry of the cell.

Results

Isolation of the Compound. Synthesis of the 10-layer perovskite was initially attempted to make an ideal intergrowth between Ca₂Fe₂O₅ brownmillerite and YBa₂Fe₃O₈ structure types, with stoichiometric amounts of BaCO₃, CaCO₃, Y₂O₃ and Fe₂O₃, adjusting the cationic ratio to a Ba₂Ca₂YFe₅ composition. Firing at 1200 °C allowed the observation of a low angle peak at $d_{hkl} \approx 9.5$ Å in the powder X-ray diffraction pattern, which was assigned to a phase with long crystalline periodicity. Referring to the previously reported Ba₂Ca₂Nd₂Fe₆O_{15.6}, the majority of diffraction peaks could be indexed on the basis of an orthorhombic perovskite superstructure with the unit cell $a_p\sqrt{2} \times 10a_p \times a_p\sqrt{2}$, in the *Imma* space group. The main impurity was BaFeO_{3- δ} which remained after several cycles of regrinding and firing, suggesting an EDS study to determine the main phase composition, before possible modifications of synthesis conditions. This analysis performed on 20 crystals of the targeted phase revealed an average cation content of Ba_{1.81}Ca_{2.32}Y_{0.87} on the A site and syntheses were targeted at this Ba, Y-deficient and Ca excess composition range.

The Ba_{1.7}Ca_{2.4}Y_{0.9}Fe₅ nominal stoichiometry allowed us to obtain a single-phase sample in a reproducible way, with a powder X-ray diffraction pattern totally indexed by the aforementioned crystallographic unit cell, characteristic of a large perovskite superstructure. It should be noted that the material could only be isolated reproducibly for this cation content under ambient conditions, suggesting a narrow, if not fixed, range of composition under the synthesis conditions. Hence, samples with A site compositions of the form Ba_{1.7+ x} Ca_{2.4- y} Y_{0.9- z} , Ba_{1.7- y} Ca_{2.4+ x} Y_{0.9- z} , Ba_{1.7- z} Ca_{2.4- y} Y_{0.9+ x} ($x, y, z > 0$; $x = y + z$) repeatedly led, respectively, to the observation of BaFeO_{3- δ} or BaFe₂O₄, Ca₂Fe₂O₅, and Y₂O₃ secondary phases. Finally, EDS performed on a 5 g sample preparation dedicated to the powder neutron diffraction experiment gave the composition Ba_{1.62}Ca_{2.32}Y_{1.06}Fe_{5.10}, with up to 0.2 variations being observed on these formula unit numbers from one crystallite to another.

(21) Rodriguez-Carvajal, J. Fullprof: A Program for Rietveld Refinement and Pattern Matching Analysis. In *Collected Abstracts of Powder Diffraction Meeting*; Toulouse, France, July 1990; Galy, J., Ed.; International Union of Crystallography: Chester, U.K., 1990; p 127.

(22) Brown, I. D.; Altermatt, D. *Acta Crystallogr., Sect. B* **1985**, *41*, 244–247.

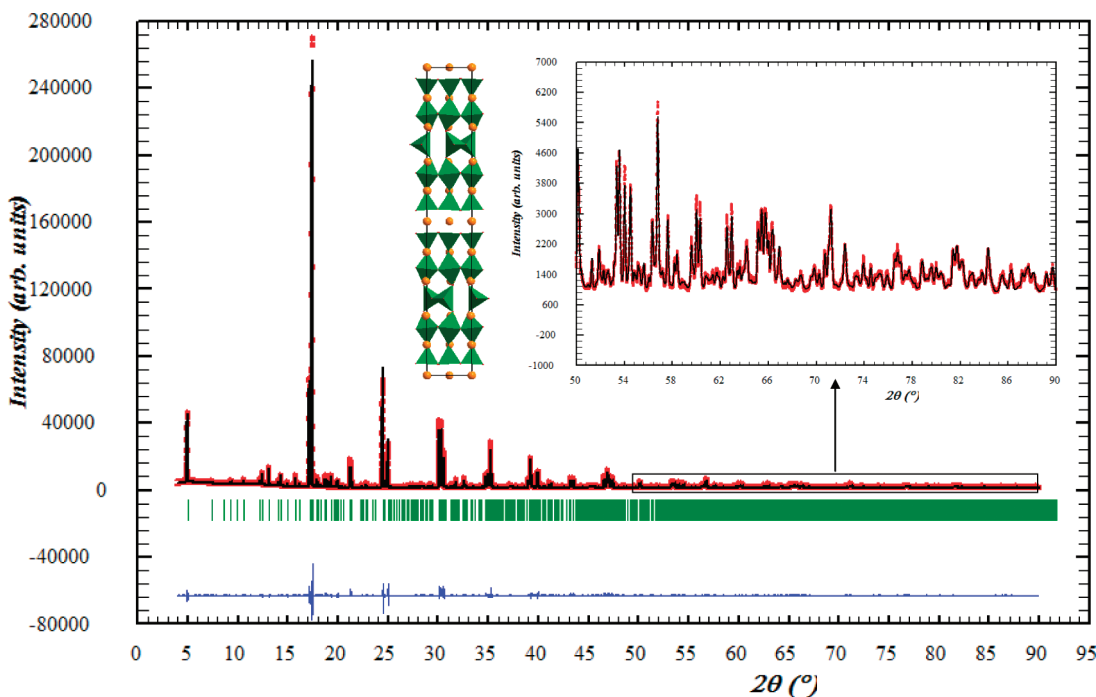


Figure 2. Rietveld refinement of the powder synchrotron X-ray diffraction data from $\text{Ba}_{1.6}\text{Ca}_{2.3}\text{Y}_{1.1}\text{Fe}_5\text{O}_{13}$ at room temperature.

Structural Analysis. Room-temperature synchrotron powder X-ray diffraction was initially performed to study the crystal structure of the new material. The unit-cell indexing and phase purity were initially confirmed with LeBail fits, using a pseudo-Voigt peak shape, giving $\chi^2 = 1.81$. Then, a $\text{Ba}_2\text{Ca}_2\text{Nd}_2\text{Fe}_6\text{O}_{15.6}$ 10-layer type model was introduced and cell parameters, atomic positions and isotropic thermal factors were refined. Final reliability factors were $R_{\text{Bragg}} = 4.19\%$, $R_p = 5.39\%$, $R_{\text{wp}} = 6.99\%$, $\chi^2 = 2.37$, for $R_{\text{exp}} = 4.54\%$. The final calculated, observed, and difference curves are presented (Figure 2), whereas structural parameters are summarized in the Supporting Information (Table SI2). These analyses confirmed the ten layer perovskite stacking, described as a regular intergrowth between $\text{YBa}_2\text{Fe}_3\text{O}_8$ and $\text{Ca}_2\text{Fe}_2\text{O}_5$ structure types, with oxygen vacancy ordering generating three types of iron environments in layers along the b axis, tetrahedral, square-based pyramidal, and octahedral, respectively, in ratios 1:2:2 with bond valence sum calculations leading to 2.87, 2.79, and 3.15, notably close to Fe^{3+} . The metal site geometries are clearly distinct from the air sensitive $\text{Ba}_2\text{Ca}_2\text{Nd}_2\text{Fe}_6\text{O}_{15.6}$ at the level of the tetrahedra, where B.V.S analysis leads to 2.27 (or 1.95 if alternatively considered as trigonal planar), whereas square-based pyramidal and octahedral sites show similar values of 2.64 and 3.11, respectively. No extra oxygen was detected in the tetrahedral layer, nor in the apical vacant site that results in the square based pyramid coordination. When forcing an oxygen position into this 0 0 1/2 site, occupancy was refined to a value of -0.013 .

Three distinct A sites were also observed with coordination numbers of 8, 9, and 12 in respective ratios 1:2:2. At this stage Ba, Ca and Y occupancies on each of these sites could not be refined due to a lack of information, and combined X-ray/neutron analysis was needed to discuss

their ordering in the crystal structure. However, estimation of the scattering intensity in terms of Barium fractional occupancy led to the different values of 0.517(2), 0.410(2), 0.907(3) for the 8, 9, and 12 coordinated sites, respectively. This could clearly be illustrated by the Fourier observed maps of the unit cell (see Figure SI1 in the Supporting Information), suggesting a preferential ordering of A site cations in the different rock salt layers occurring along the stacking axis b .

Powder X-ray diffraction patterns were collected up to 900 °C (after which the material reacts with the quartz capillary), with a step of 100 °C, to evaluate possible structural changes over this temperature range (Figure 3). Except for the thermal expansion and broadening of peaks, the 900 °C pattern showed a striking similarity with the room temperature one and the a , b , and c parameters undergo a linear increase upon heating. An anisotropic thermal expansion was observed: although a and c parameters nearly follow a parallel evolution, the long b axis increases almost twice as rapidly, suggesting that the different successive layers tend to constrain each other in the basal plane (ac) while relaxing more easily along the stacking axis b . This anisotropic thermal expansion between the basal plane and stacking axis is seen in other layered structures like Na_xCoO_2 ,²³ or in the related $\text{YBa}_2\text{Cu}_3\text{O}_7$.²⁴ The unit-cell volume expansion is also linear, and these observed effects show there is no structural change or significant oxygen content evolution from room temperature to 900 °C. Thermogravimetric analysis in an air atmosphere confirmed these features,

(23) dos Santos, C. A. M.; Neumeier, J. J.; Yu, Yi-Kuo; Bollinger, R. K.; Jin, R.; Mandrus, D.; Sales, B. C. *Phys. Rev. B* **2006**, *74*, 132402.

(24) Meingast, C.; Kraut, O.; Wolf, T.; Wühl, H. *Phys. Rev. Lett.* **1991**, *67*, 1634–1637.

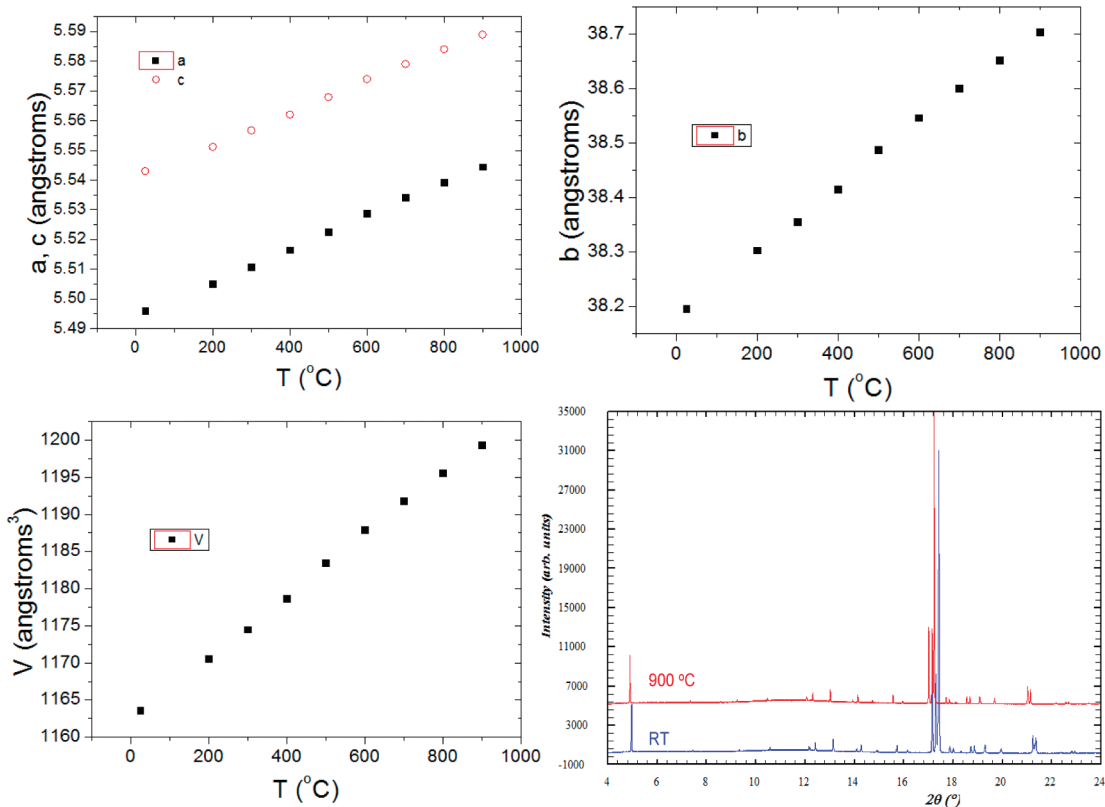


Figure 3. Evolution of the unit-cell parameters of $\text{Ba}_{1.6}\text{Ca}_{2.3}\text{Y}_{1.1}\text{Fe}_5\text{O}_{13}$ as a function of temperature.

with the sample showing no weight loss or gain outside of the error range of the measurement (0.1 oxygen per formula unit i.e. 0.02 when normalized to an ABO_3 formula unit), when heated and cooled back from room temperature to 1000 °C. The diagonal tensor for thermal expansion then has coefficients $\alpha_{11} = 9.8 \times 10^{-6} \text{ K}^{-1}$, $\alpha_{22} = 15.4 \times 10^{-6} \text{ K}^{-1}$ and $\alpha_{33} = 10.2 \times 10^{-6} \text{ K}^{-1}$, along a , b , and c , respectively, resulting in a volumetric thermal expansion coefficient $\alpha_v = \alpha_{11} + \alpha_{22} + \alpha_{33} = 35.4 \times 10^{-6} \text{ K}^{-1}$ over the range 25–900 °C. The phase stability in CO_2 was evaluated by annealing the sample under pure CO_2 at 700 °C for 24 h. The material remained unchanged after this treatment, in contrast to some other Ba-containing candidate cathode materials.^{25–27}

Powder neutron diffraction patterns were also collected at variable temperature. Room-temperature data were analyzed with the model determined by X-ray diffraction and showed some peaks for which the intensity could not be fitted, although the d spacing was characteristic of the unit cell. Data collected at 450 °C showed a clear decrease in the intensity of these peaks relative to the rest of the diffraction diagram, and data collected with a step of 5 °C showed this evolution until 480 °C, after which temperature the decrease stops (see Figure SI2 in the Supporting Information). The intensity mismatch between calculated

and experimental curves at room temperature was therefore attributed to magnetic scattering and the magnetic transition temperature was in the range 480–485 °C.

To assess the cation ordering in the structure, we first chose to remove the effect of the magnetic Bragg scattering by analyzing the data above the magnetic ordering temperature, and carried out combined X-ray/neutron analysis on a 485 °C PND diagram and a 500 °C PXD diagram. Unit-cell parameters were allowed to refine freely between the two sets of data while all the atomic parameters were considered identical, which we consider a sensible assumption, given the small temperature difference and the observations made during the variable temperature PXD experiment. The structural model was refined using the results of the previous characterizations, this time with the introduction of all A site cations. The *Imma* space group leads to an average model for the iron tetrahedral chains with two possible orientations, each present with a fraction of 50% (see Figure SI3 in the Supporting Information). Because of the more sensitive detection of oxygen scattering by neutron diffraction, the *I2mb* space group, with ordered tetrahedral orientations, was also tested for the structure determination. However, the refinement could not be stabilized when refining 6 of the 7 oxygen positions, which change from special to general positions with the change from *Imma* to *I2mb*. Moreover, Fourier difference maps show the two different tetrahedral orientations in the *I2mb* model, which then also leads to an average disordered structure. Neither of the two iron sites generated by these two orientations could be stably refined. These considerations

(25) Tarancón, A.; Peña-Martínez, J.; Marrero-López, D.; Morata, A.; Ruíz-Morales, J. C.; Núñez, P. *Solid State Ionics* **2008**, *179*, 2372–2378.
 (26) Arnold, M.; Wang, H.; Feldhoff, A. *J. Membr. Sci.* **2007**, *293*, 44–52.
 (27) Yáng, Z.; Harvey, A. S.; Gauckler, L. J. *Scr. Mater.* **2009**, *61*, 1083–1086.

Table 1. Structural parameters of $\text{Ba}_{1.6}\text{Ca}_{2.3}\text{Y}_{1.1}\text{Fe}_5\text{O}_{13}$ from combined refinements above the Néel transition temperature; unconstrained refined content for the A site cations is $\text{Ba}_{1.9}\text{Ca}_{2.1}\text{Y}$ as discussed in the Text^a

| atom | multiplicity | occupancy | x | y | z | $B_{\text{iso}} (\text{\AA}^{-2})$ |
|------|--------------|----------------|-----------|------------|------------|------------------------------------|
| Fe1 | 8h | 1 | 0 | 0.04934(1) | 0.5055(3) | 0.61(2) |
| Fe2 | 8h | 1 | 0 | 0.15307(1) | 0.5066(2) | 0.84(2) |
| Fe3 | 8i | 0.5 | 0.0611(3) | 1/4 | 0.5740(3) | 0.33(3) |
| O1 | 8g | 1 | 1/4 | 0.03914(3) | 1/4 | 2.28(5) |
| O2 | 8g | 1 | 1/4 | 0.96318(3) | 1/4 | 1.14(4) |
| O3 | 8g | 1 | 1/4 | 0.15099(4) | 1/4 | 1.27(4) |
| O4 | 8g | 1 | 1/4 | 0.65833(3) | 1/4 | 1.31(4) |
| O5 | 8i | 0.5 | 0.4001(5) | 1/4 | 0.6093(6) | 1.54(6) |
| O6 | 8h | 1 | 0 | 0.09801(3) | 0.5179(4) | 1.66(3) |
| O7 | 8h | 1 | 0 | 0.20811(3) | 0.4391(4) | 2.48(5) |
| Ba1 | 4a | 0 ^b | 0 | 0 | 0 | 1.38(4) |
| Ca1 | 4a | 0.34(1) | 0 | 0 | 0 | 1.38(4) |
| Y1 | 4a | 0.66(1) | 0 | 0 | 0 | 1.38(4) |
| Ba2 | 8h | 0.90(1) | 0 | 0.59981(1) | -0.0043(3) | 1.92(2) |
| Ca2 | 8h | 0.08(1) | 0 | 0.59981(1) | -0.0043(3) | 1.92(2) |
| Y2 | 8h | 0.02(1) | 0 | 0.59981(1) | -0.0043(3) | 1.92(2) |
| Ba3 | 8h | 0.05(1) | 0 | 0.69313(2) | -0.0232(4) | 1.32(4) |
| Ca3 | 8h | 0.80(1) | 0 | 0.69313(2) | -0.0232(4) | 1.32(4) |
| Y3 | 8h | 0.15(1) | 0 | 0.69313(2) | -0.0232(4) | 1.32(4) |

^aSpace group: *Imma*, $a = 5.5318(3) \text{\AA}$, $b = 38.569(2) \text{\AA}$, $c = 5.5776(3) \text{\AA}$. ^b–0.03 when refined.

Table 2. Principal Fe–O and A–O distances (Å) for the different sites and principal O–Fe–O angles in Fe polyhedra and bridging Fe–O–Fe angles from the combined refinement of $\text{Ba}_{1.6}\text{Ca}_{2.3}\text{Y}_{1.1}\text{Fe}_5\text{O}_{13}$ above the Néel transition temperature

| bond | $n \times$ distance (Å) | bond | $n \times$ distance (Å) |
|------------------------|-------------------------|------------------------|-------------------------|
| (Fe1)–(O1) | 2 × 2.0243(8) | (A2)–(O1) | 2 × 3.0440(14) |
| (Fe1)–(O2) | 2 × 2.0015(8) | (A2)–(O2) | 2 × 3.1347(14) |
| (Fe1)–(O6) | 1.8784(17) | (A2)–(O3) | 2 × 2.7726(13) |
| | | (A2)–(O4) | 2 × 3.0031(14) |
| (Fe2)–(O3) | 2 × 1.9918(7) | (A2)–(O6) | 2 × 2.76952(10) |
| (Fe2)–(O4) | 2 × 1.9485(7) | (A2)–(O6) | 2.865(2) |
| (Fe2)–(O6) | 2.1247(17) | (A2)–(O6) | 2.714(2) |
| (Fe2)–(O7) | 2.1558(14) | | |
| | | (A3)–(O3) | 2 × 2.4808(15) |
| (Fe3)–(O5) | 1.885(3) | (A3)–(O4) | 2 × 2.4568(15) |
| (Fe3)–(O5) | 1.979(3) | (A3)–(O5) | 2 × 2.3796(16) |
| (Fe3)–(O7) | 2 × 1.8141(13) | (A3)–(O7) | 2 × 2.8334(4) |
| | | (A3)–(O7) | 2.391(2) |
| (A1)–(O1) | 4 × 2.4770(9) | | |
| (A1)–(O2) | 4 × 2.4235(9) | | |
| $n \times$ angle (deg) | | $n \times$ angle (deg) | |
| (O1)–(Fe1)–(O1) | 86.18(3) | (O5)–(Fe3)–(O5) | 110.8(2) |
| (O1)–(Fe1)–(O2) | 2 × 154.80(3) | (O5)–(Fe3)–(O7) | 2 × 103.23(16) |
| (O1)–(Fe1)–(O2) | 2 × 87.75(3) | (O5)–(Fe3)–(O7) | 2 × 106.63(17) |
| (O1)–(Fe1)–(O6) | 2 × 102.72(10) | (O7)–(Fe3)–(O7) | 125.90(11) |
| (O2)–(Fe1)–(O2) | 87.41(3) | | |
| (O2)–(Fe1)–(O6) | 2 × 102.47(10) | (Fe1)–(O1)–(Fe1) | 157.58(7) |
| | | (Fe1)–(O2)–(Fe1) | 152.07(7) |
| (O3)–(Fe2)–(O3) | 87.94(3) | (Fe2)–(O3)–(Fe2) | 175.37(6) |
| (O3)–(Fe2)–(O4) | 2 × 90.69(3) | (Fe2)–(O4)–(Fe2) | 168.06(6) |
| (O3)–(Fe2)–(O4) | 2 × 176.04(3) | (Fe3)–(O5)–(Fe3) | 122.77(6) |
| (O3)–(Fe2)–(O6) | 2 × 88.91(9) | (Fe1)–(O6)–(Fe2) | 176.19(9) |
| (O3)–(Fe2)–(O7) | 2 × 85.08(7) | (Fe2)–(O7)–(Fe3) | 143.56(7) |
| (O4)–(Fe2)–(O4) | 90.43(3) | | |
| (O4)–(Fe2)–(O6) | 2 × 94.78(9) | | |
| (O4)–(Fe2)–(O7) | 2 × 91.10(8) | | |
| (O6)–(Fe2)–(O7) | 171.64(12) | | |

show that the *Imma* space group is preferred for the determination of cation ordering in the structure.

First, Ba, Ca, and Y were fixed at arbitrary occupations in the different A sites with Ca and Ba introduced initially in the sites showing weaker and stronger X-ray scattering, respectively. Atomic as well as thermal parameters could be successively refined for all positions. We were able to

refine the cation occupancy on each A site with the only constraint applied being a total occupancy of one for each site. One should note that neutron scattering lengths are respectively 4.70, 7.75, and 5.07 pm for Ca, Y, and Ba. Hence, Ba and Ca possess particularly close neutron scattering factors. However, the distinction between Ca^{2+} and Ba^{2+} is clearly resolved by X-ray scattering factors, the two cations containing respectively 18 and 54e[–], which yields a 1/3 ratio, whereas Y^{3+} has 36e[–]. Results for the eight-coordinate site gave the composition $\text{Ba}_{-0.03}\text{Ca}_{0.40}\text{Y}_{0.63}$, and we therefore considered this layer as Ba-free to obtain the final results: $\text{Ca}_{0.34(1)}\text{Y}_{0.66(1)}$ for the eight-coordinate site; $\text{Ba}_{0.05(1)}\text{Ca}_{0.80(1)}\text{Y}_{0.15(1)}$ for the nine-coordinate site; $\text{Ba}_{0.90(1)}\text{Ca}_{0.08(1)}\text{Y}_{0.02(1)}$ for the twelve-coordinate site.

This confirms the strong preferential ordering indicated by the X-ray diffraction study. Barium is located almost exclusively on the 12-coordinate site, which is associated with the observation of longer A–O distances (Table 2), in agreement with the larger Ba^{2+} ionic radius compared to Ca^{2+} or Y^{3+} . On the other hand, the nine-coordinate site strongly favors the presence of calcium, whereas the eight-coordinate site results in an oxygen- and barium-free mixed Ca/Y layer, as observed in numerous copper oxides (Figure 5).^{28,29} In parallel, oxygen sites were refined to occupancies of 0.97(1), 1.05(1), 0.95(1), 1.02(1), 0.50(1), 1.01(1), and 0.97(1) for O1, O2, O3, O4, O5, O6, and O7, respectively, and for such small deviations were considered to be all fully occupied, except for O5 associated with the tetrahedral chain disorder discussed above (see Figure SI3 in the Supporting Information), which was considered half occupied. No extra oxygen could be detected in the Fourier difference maps.

(28) Parise, J. B.; McCarron, E. M. *J. Solid State Chem.* **1989**, *83*, 188–197.
 (29) Fjellvag, H.; Morita, Y.; Nagai, T.; Lee, J. H.; Chen, J. M.; Liu, R. S.; Hauback, B. C.; Awana, V. P. S.; Matsui, Y.; Yamauchi, H.; Karppinen, M. *J. Solid State Chem.* **2006**, *179*, 632–645.

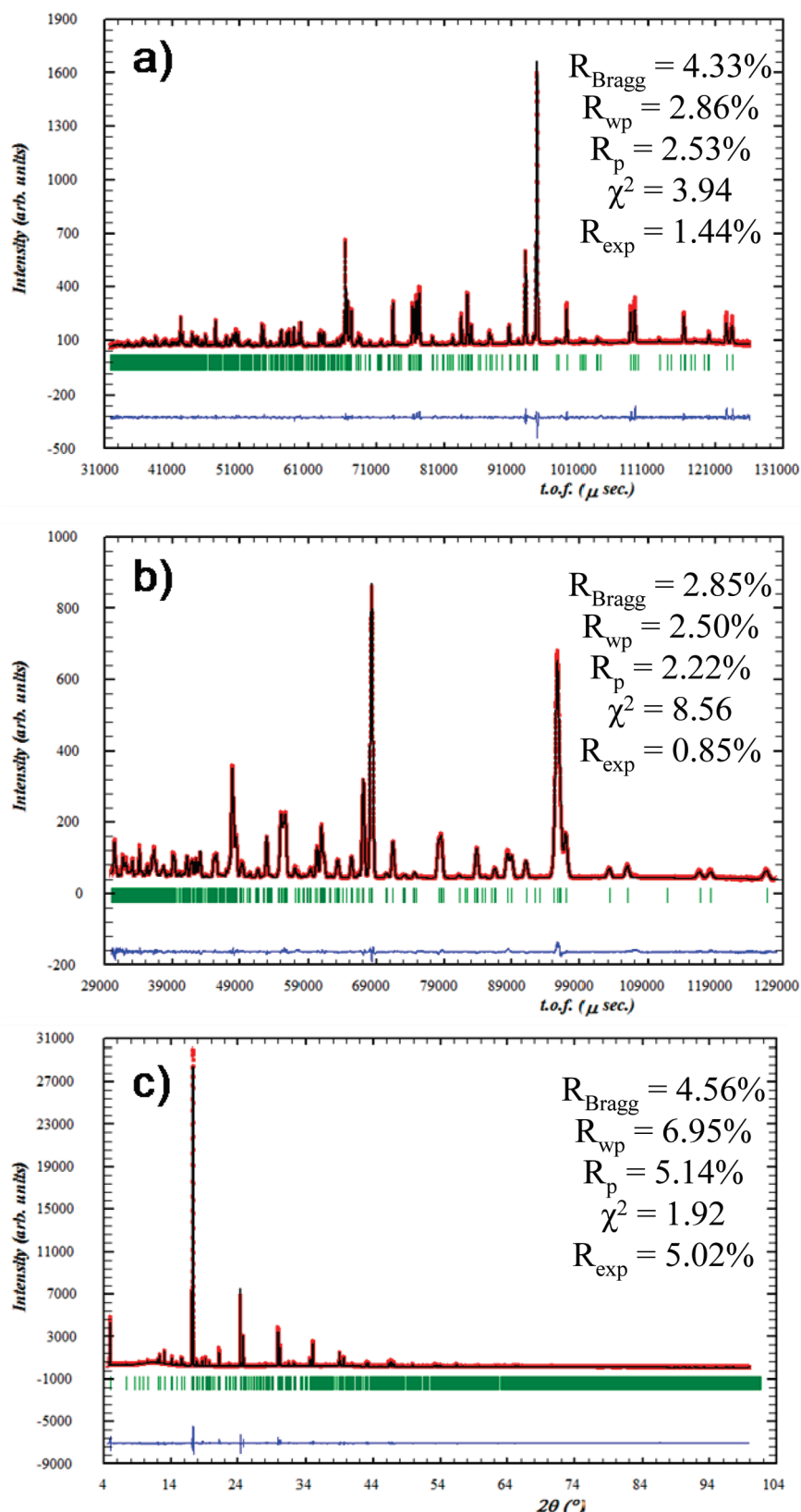


Figure 4. Combined X-ray and neutron refinements of $\text{Ba}_{1.6}\text{Ca}_{2.3}\text{Y}_{1.1}\text{Fe}_5\text{O}_{13}$ at 485 and 500 $^{\circ}\text{C}$ respectively. (a) Neutron backscattering bank, (b) neutron 90° bank, (c) synchrotron X-rays.

In that sense, this compound shows a distinct behavior when compared to the parent $\text{Ba}_2\text{Ca}_2\text{Nd}_2\text{Fe}_6\text{O}_{15.6}$, where partial occupancy of oxygen sites—ideally fully vacant in the perfect intergrowth—in the equatorial plane of the

tetrahedra can be observed at 500 $^{\circ}\text{C}$, accompanied/compensated by an oxygen deficiency at the level of the apical oxygen of these tetrahedra. This phenomenon was associated with a high-temperature order-disorder transition

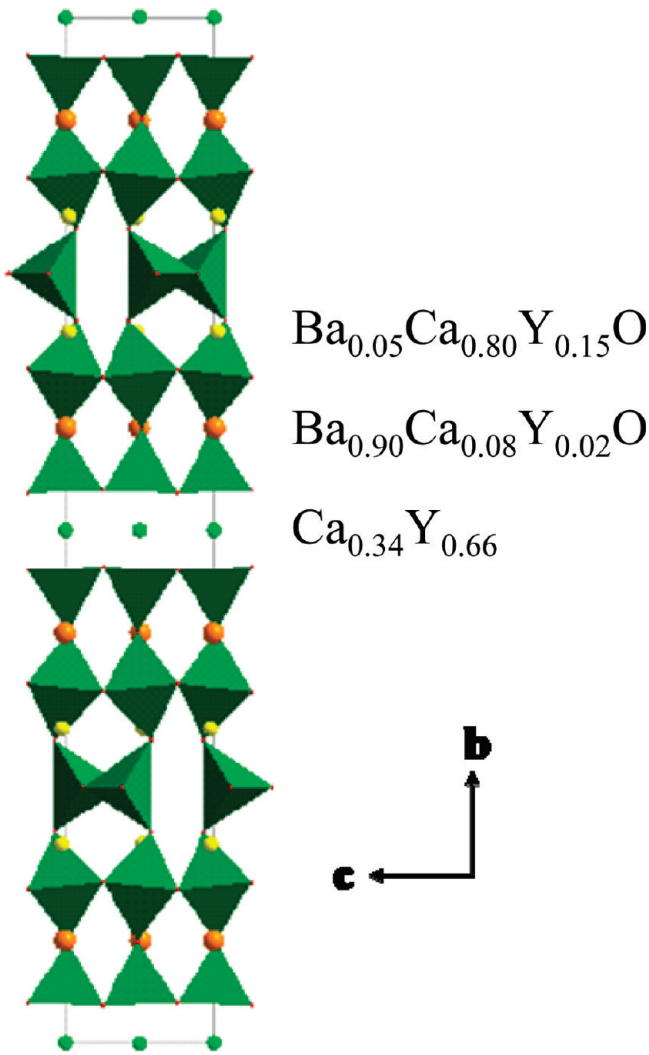


Figure 5. Structure of $\text{Ba}_{1.6}\text{Ca}_{2.3}\text{Y}_{1.1}\text{Fe}_5\text{O}_{13}$ showing the composition of the rock salt layers. The combined refinement leads to a total A site composition of $\text{Ba}_{1.9}\text{Ca}_{2.1}\text{Y}$.

similar to those reported for brownmillerite materials.^{30,31} In the present case, the absence of this transition is not only evidenced by the refined occupancies and Fourier difference maps but also by the previously discussed linear evolution of cell parameters over the range RT-900 °C. Structural parameters and interatomic distances are summarized (Tables 1 and 2), whereas the experimental, calculated, and difference curves are also presented for each of the high-temperature refinements (Figure 4), accompanied with reliability factors for each data bank.

From these refinements, the composition of the phase is $\text{Ba}_{1.90}\text{Ca}_{2.10}\text{Y}_{1.00}\text{Fe}_5\text{O}_{13}$, which leads to a pure Fe^{3+} compound with a perovskite superstructure (Figure 5). One should note that the only constraint applied to the refined A site composition was the total occupancy of each site, and therefore we can consider this formula in good agreement with the EDS results $\text{Ba}_{1.62}\text{Ca}_{2.32}\text{Y}_{1.06}\text{Fe}_{5.10}$ or the nominal composition $\text{Ba}_{1.7}\text{Ca}_{2.4}\text{Y}_{0.9}\text{Fe}_5$. Furthermore,

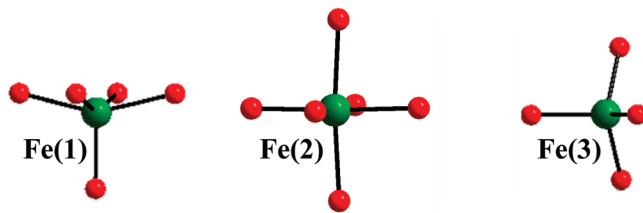


Figure 6. Iron polyhedra deduced from the combined refinement of $\text{Ba}_{1.6}\text{Ca}_{2.3}\text{Y}_{1.1}\text{Fe}_5\text{O}_{13}$.

tests of composition fixed to the EDS or nominal contents did not have major impacts on the reliability factors of the structural refinement, which could explain the observed difference in derived compositions. Because X-ray or neutron diffraction are not the most reliable techniques for chemical composition analysis, the A site composition will be addressed in the following parts by the EDS analysis assignment, resulting in the formula $\text{Ba}_{1.6}\text{Ca}_{2.3}\text{Y}_{1.1}\text{Fe}_5\text{O}_{13}$ ($\text{Fe}^{+2.98}$, consistent with the Mössbauer observations discussed later), considering as well that maximal deviations of 0.2 were observed on these formula unit numbers by this technique.

Iron coordination polyhedra are shown in Figure 6. From the high-temperature combined refinements, bond valence sum (B.V.S.) calculations lead to 2.99, 2.75, and 2.98 for the tetrahedral, square-based pyramidal and octahedral sites respectively. Remarkably, a shortening of the apical Fe–O distances is observed for the 4 and 5 coordinate sites (1.81 and 1.88 Å), as opposed to an extension for the 6 coordinate site (2.12 and 2.18 Å). This difference is not found at the level of the equatorial distances with limiting values of 1.88 (for the tetrahedra) and 2.02 Å (for the square-based pyramid). This phenomenon is also observed in the parent $\text{YBa}_2\text{Fe}_3\text{O}_8$ and $\text{Ca}_2\text{Fe}_2\text{O}_5$ materials^{32,33} and emphasizes the perovskite structure flexibility, which plays a crucial role in the stabilization of this ten layered stacking. On the other hand, in $\text{Nd}_2\text{Ba}_2\text{Ca}_2\text{Fe}_6\text{O}_{15.6}$, obtained under highly reducing conditions, a trigonal planar environment accommodating Fe^{2+} was suggested because of significant bond length and angle discrepancies for the ideal tetrahedral arrangement. In the present case this possible interpretation of our refined model would lead to one extremely short Fe–O equatorial distance (1.78 Å), while reducing the BVS to 2.66. The tetrahedral arrangement is favored in the present Fe^{3+} compound, supported as well by a less distorted tetrahedral geometry (mainly at the level of bond angles) than in the case of $\text{Nd}_2\text{Ba}_2\text{Ca}_2\text{Fe}_6\text{O}_{15.6}$, where the presence of nonspherical Fe^{2+} on this site drives the lowering of the symmetry of the polyhedra. For example, if one consider a tetrahedral site in $\text{Nd}_2\text{Ba}_2\text{Ca}_2\text{Fe}_6\text{O}_{15.6}$ bond angles of 97 and 115° are observed for the shortest contacts, while their equivalents are 103 and 107° in $\text{Ba}_{1.6}\text{Ca}_{2.3}\text{Y}_{1.1}\text{Fe}_5\text{O}_{13}$, confirming the distinction of the two environments. As for the pyramidal and octahedral sites, no such significant difference can be observed

(30) Berastegui, P.; Hull, S.; Garcia-Garcia, F. J.; Eriksson, S. G. *J. Solid State Chem.* **2002**, *164*, 119–130.

(31) Schmidt, M.; Campbell, S. J. *J. Solid State Chem.* **2001**, *156*, 292–304.

(32) Karen, P.; Suard, E.; Fauth, F. *Inorg. Chem.* **2005**, *44*, 8170–8172.

(33) Colville, A. A. *Acta Crystallogr., Sect. B* **1970**, *26*, 1469.

between the two compounds, with respective bond valence sums of 2.64 and 3.11 in the reduced Nd-containing compound (2.75 and 2.98 in the present case). The geometry of these square based pyramids and octahedra compares well in both structures with a shorter apical bond found in the square based pyramid, and two longer apical bonds found in the octahedra. These findings confirm that the lowest coordinated site is most probably the host for Fe^{2+} in $\text{Nd}_2\text{Ba}_2\text{Ca}_2\text{Fe}_6\text{O}_{15.6}$, and that this site is oxidized to Fe^{3+} in $\text{Ba}_{1.6}\text{Ca}_{2.3}\text{Y}_{1.1}\text{Fe}_5\text{O}_{13}$, whereas Fe1 and Fe2 remain similar environments, containing Fe^{3+} in both compounds.

After the determination of the A site ordering by combining X-ray and neutron diffraction techniques above the magnetic transition temperature, room temperature PND data were analyzed to access the magnetic structure of the compound. The cation composition was fixed according to the previous refinements. Magnetic scattering grows on top of the nuclear Bragg scattering (propagation vector $k = 0$), which indicates that the magnetic unit cell is the same as the crystallographic unit cell. Considering a G-type antiferromagnetic structure with constant, staggered moments (anti)parallel to the a axis allowed fitting of the magnetic contribution to the Bragg reflections. This suggests that irrespective of the Fe coordination, the ordering is simply stabilized by anti-ferromagnetic nearest neighbor Fe^{3+} – Fe^{3+} superexchange interactions, and we therefore made the assumption that these moments were of the same amplitude on all sites. Thus, the magnetic structure of this compound is closely related to those of parent Fe^{3+} compounds such as $\text{YBa}_2\text{Fe}_3\text{O}_8$,³² $\text{LnCa}_2\text{Fe}_3\text{O}_8$ ($\text{Ln} = \text{La, Nd}$)³⁴ or brownmillerites like $\text{Sr}_2\text{Fe}_2\text{O}_5$ ³⁵ and $\text{Ca}_2\text{Fe}_2\text{O}_5$,³⁶ where the same type of order is observed, with a similar direction for the magnetic moments, orthogonal to the stacking axis. The refined amplitude of the ordered moments of $3.638(9)\mu_{\text{B}}$ is also comparable to the above cited materials, in agreement with the moment reduction predicted by the Brillouin curve for $S = 5/2$ when $T/T_{\text{N}} \sim 0.4$. For example, in $\text{LaCa}_2\text{Fe}_3\text{O}_8$, which has a T_{N} of 735 K, compared to 750 K in the present case, the refined value is $3.4 \pm 0.2 \mu_{\text{B}}$ at room temperature.³⁴ These results are also in agreement with the G-type antiferromagnetic order found to be most stable by theoretical calculations and discussed later, with a similar amplitude of the magnetic moments. Interestingly, introducing a two-phase model for this room temperature refinement considerably improved the agreement between experimental and calculated profiles of the high resolution back scattering bank, particularly making a dramatic impact on the peak asymmetry. In order to avoid an increase of the number of refined parameters, the structural models for the two nuclear (magnetic) phases need to be fully

constrained to have the same atomic parameters (positional, magnetic moments), with only cell parameters or peak broadening parameters allowed to vary. Therefore, the model consists of two $\text{Ba}_{1.9}\text{Ca}_{2.1}\text{YFe}_5\text{O}_{13}$ 10-layer cells with the same crystal and magnetic structures. The refined respective unit cells of each phase are $5.4970(2) \times 38.254(2) \times 5.5439(2) \text{ \AA}^3$ and $5.5072(2) \times 38.204(2) \times 5.5482(2) \text{ \AA}^3$ and their phase fractions are 0.63 and 0.37. Here we should point out the extremely small difference of 0.07, 0.13, and 0.08% for a , b , and c and rather than truly containing two phases, the refinement procedure, which improves the overall profile and the individual peak shapes, should be considered as an efficient though artificial way to deal with the highly probable presence of defects such as stacking faults and composition heterogeneities in the material, given the layered structure combined with the presence of five distinct elements. This feature was only clearly observed on the high resolution back scattering bank, and was not required to obtain a satisfactory fit to the 485 °C refinement, which is certainly associated with broadening slightly decreasing peak resolution at higher temperatures, thus allowing averaging of the presence of defects with a one phase refinement. The final observed, calculated and difference profiles are presented (Figure 7), along with an illustration of the magnetic structure (Figure 8).

Mössbauer analysis performed at 77 and 298K revealed complex spectra (Figure 9), with multiple sets of six line patterns, consistent with a magnetically ordered sample. According to the crystal structure determination, the patterns were fitted using the 2:2:1 site ratio for Fe1, Fe2 and Fe3. At room temperature, chemical shifts of 0.32 and 0.34 mm s^{-1} for Fe1 and Fe2 are consistent with Fe^{3+} in square pyramidal and octahedral environment respectively. The value of 0.2 mms^{-1} for Fe3 is consistent with the same oxidation state in a tetrahedral environment, as compared to 0.20 mm s^{-1} for Fe^{3+} in the tetrahedral site of $\text{Ca}_2\text{Fe}_2\text{O}_5$.³⁷ Here we should note that if Fe1 and Fe2 crystallographic sites are slightly more difficult to differentiate because of their equal multiplicity and similar Mössbauer chemical shifts, the Fe3 site can clearly be identified from its distinct multiplicity compared with the two others. Hence, we can be sure this different chemical shift is attributed to the Fe site determined as tetrahedral by crystallographic analysis.

Theoretical Calculations. To gain a more detailed understanding of the electronic structure of the new material, we carried out electronic structure calculations within the framework of plane-wave-based density functional theory (DFT). We performed calculations using the VASP code,³⁸ with core electrons treated using the projector augmentor wave method³⁹ and valence electrons expanded in plane-waves with an energy cutoff of 400 eV. An exchange-correlation functional in the generalized gradient approximation (GGA)⁴⁰ was used for preliminary

(34) Hudspeth, J. M.; Goossens, D. J.; Studer, A. J.; Withers, R. L. *J. Phys.: Condens. Matter* **2009**, *21*, 124206.
 (35) Greaves, C.; Jacobson, A. J.; Tofield, B. C.; Fender, B. E. F. *Acta Crystallogr., Sect. B* **1975**, *31*, 641.
 (36) Berastegui, P.; Eriksson, S.-G.; Hull, S. *Mater. Res. Bull.* **1999**, *34*, 303–314.

(37) Mesnil, F. *J. Phys. Chem. Solids* **1985**, *46*, 763–789.
 (38) Kresse, G.; Furthmüller, J. *J. Phys. Rev. B* **1996**, *54*, 11169.
 (39) Kresse, G.; Joubert, J. *Phys. Rev. B* **1999**, *59*, 1758.
 (40) Perdew, J. P.; Chevary, J. A.; Vosko, S. H.; Jackson, K. A.; Pederson, M. R.; Singh, D. J.; Fiolhais, C. *Phys. Rev. B* **1992**, *46*, 6671–6687.

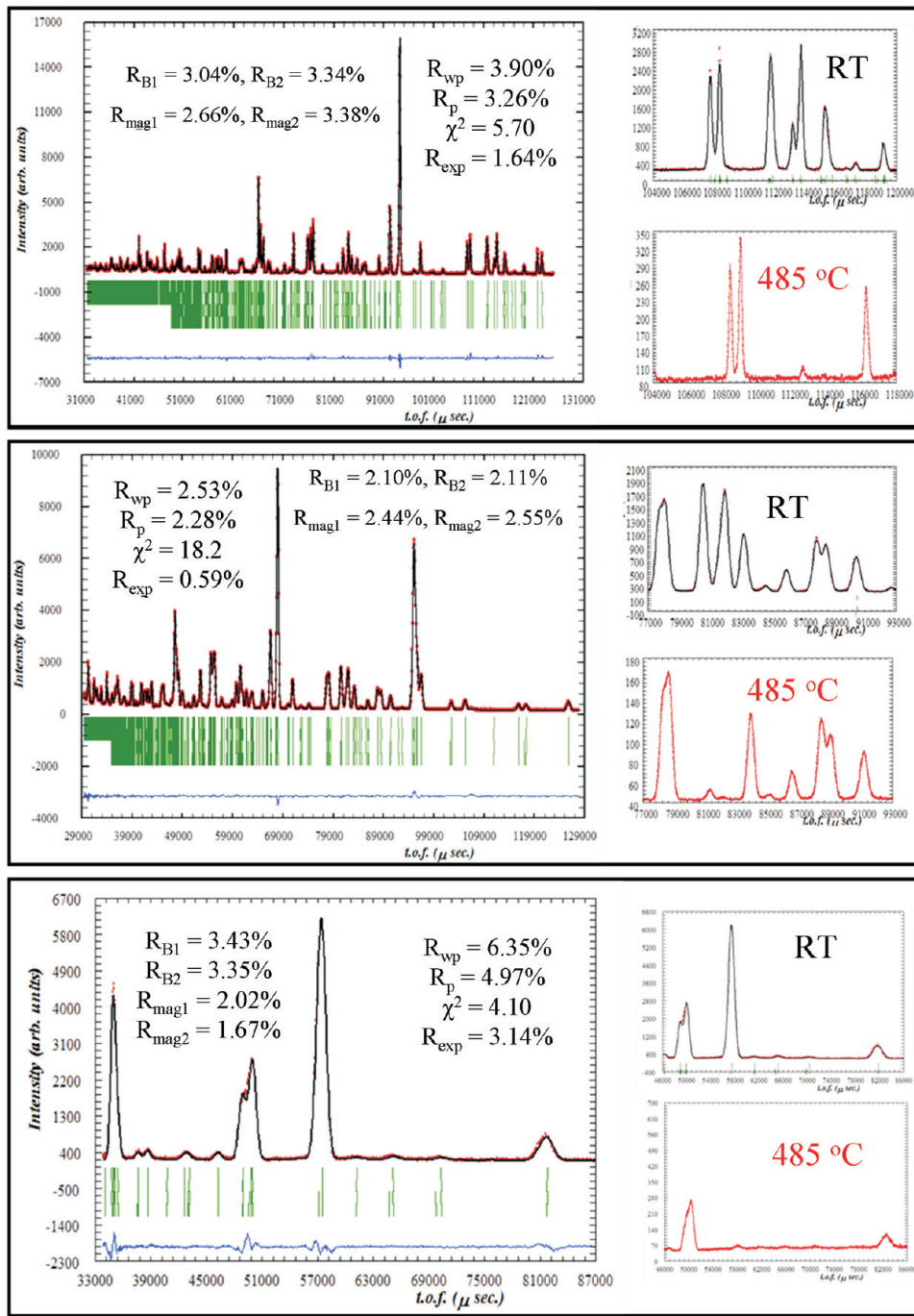


Figure 7. Room-temperature powder neutron diffraction of $\text{Ba}_{1.6}\text{Ca}_{2.3}\text{Y}_{1.1}\text{Fe}_5\text{O}_{13}$. From top to bottom: observed, calculated and difference profiles for backscattering bank, 90° bank, and 90° low-angle bank at room temperature. Intense magnetic scattering regions are compared with the same regions above T_N . The two phases consist of the previously refined compositions $\text{Ba}_{1.9}\text{Ca}_{2.1}\text{YFe}_5\text{O}_{13}$ with the same atomic parameters in both phases but different cell parameters. Profile reliability factors are presented for each data bank, and Bragg and magnetic R factors are presented for both phases in each bank.

calculations. To correct for the well-known failing of the GGA functional to describe localized d -electrons, in the calculation of the density of states, the functional was augmented with an additional onsite Coulomb term for the iron atoms, using the approach proposed by Dudarev.⁴¹ Values of 4.3 and 5.4 eV were chosen for the effective U parameter, U_{eff} , following other calculations

for Fe^{3+} oxides.^{42,43} The unit-cell parameters and atomic positions determined by refining the PXD/PND data were used for all calculations.

It was not feasible computationally to perform electronic structure calculations with the A site cations fully disordered within their layers, or with the experimentally determined fractional occupancy. Instead we performed calculations using the ideal stoichiometric composition $\text{YBa}_2\text{Ca}_2\text{Fe}_5\text{O}_{13}$, which is close to the experimentally

(41) Dudarev, S. L.; Botton, G. A.; Savrasov, S. Y.; Humphreys, C. J.; Sutton, A. P. *Phys. Rev. B* **1998**, *57*, 1505–1509.

(42) Yang, Z.; Huang, Z.; Ye, L.; Xie, X. *Phys. Rev. B* **1999**, *60*, 15674–15682.

(43) Mosey, N. J.; Liao, P.; Carter, E. A. *J. Chem. Phys.* **2008**, *129*, 014103.

determined composition, and with four different arrangements of cations on the A site positions. For the eight, nine and twelve coordinate sites these corresponded

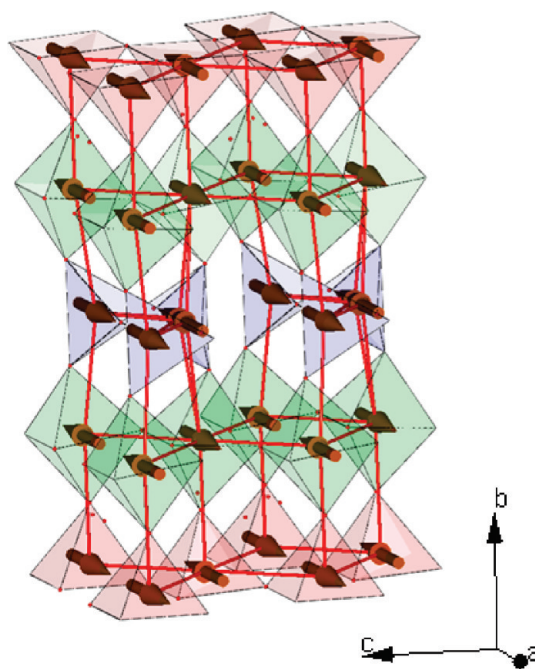


Figure 8. Magnetic structure of $\text{Ba}_{1.6}\text{Ca}_{2.3}\text{Y}_{1.1}\text{Fe}_5\text{O}_{13}$. Half of the structure is presented along b axis.

to compositions of (1) Y, Ca, Ba, (2) Y, $\text{Ba}_{0.5}\text{Ca}_{0.5}$, $\text{Ba}_{0.5}\text{Ca}_{0.5}$, (3) $\text{Y}_{0.5}\text{Ca}_{0.5}$, $\text{Y}_{0.25}\text{Ca}_{0.75}$, Ba, and (4) Y, $\text{Ba}_{0.125}\text{Ca}_{0.875}$, $\text{Ba}_{0.875}\text{Ca}_{0.125}$. We performed calculations on arrangements 1 and 2 in supercells with four formula units (FU), with k -point sampling on a $9 \times 9 \times 1$ grid, and arrangements 3 and 4 in a larger supercell with 16 FU and a $5 \times 5 \times 1$ k -point grid. The structures used can be found in the Supporting Information (Figure SI4).

After performing nonmagnetic calculations, arrangement 1 was found to be the most stable with the arrangements 2, 3, and 4 less stable by 2.52, 0.29, and 0.63 eV/FU, respectively. It is interesting to note that the three arrangements closest to the experimentally determined site occupancies have the lowest energies, though it is clear that non-spin-polarized DFT calculations are not able to correctly predict the mixing between the A site cations. Instead, it is necessary to include the magnetic interactions between the iron atoms.

Because the fully ordered system (arrangement 1) was found to be the most stable energetically for nonspin polarized calculations and is the computationally cheapest system to investigate, we have used this structure for a more in depth study of the magnetic structure of the material. We performed spin-polarized GGA calculations with ferromagnetic, A-type, C-type, and G-type antiferromagnetic orderings of the spin moments on the iron atoms. The calculated energies were lower than the

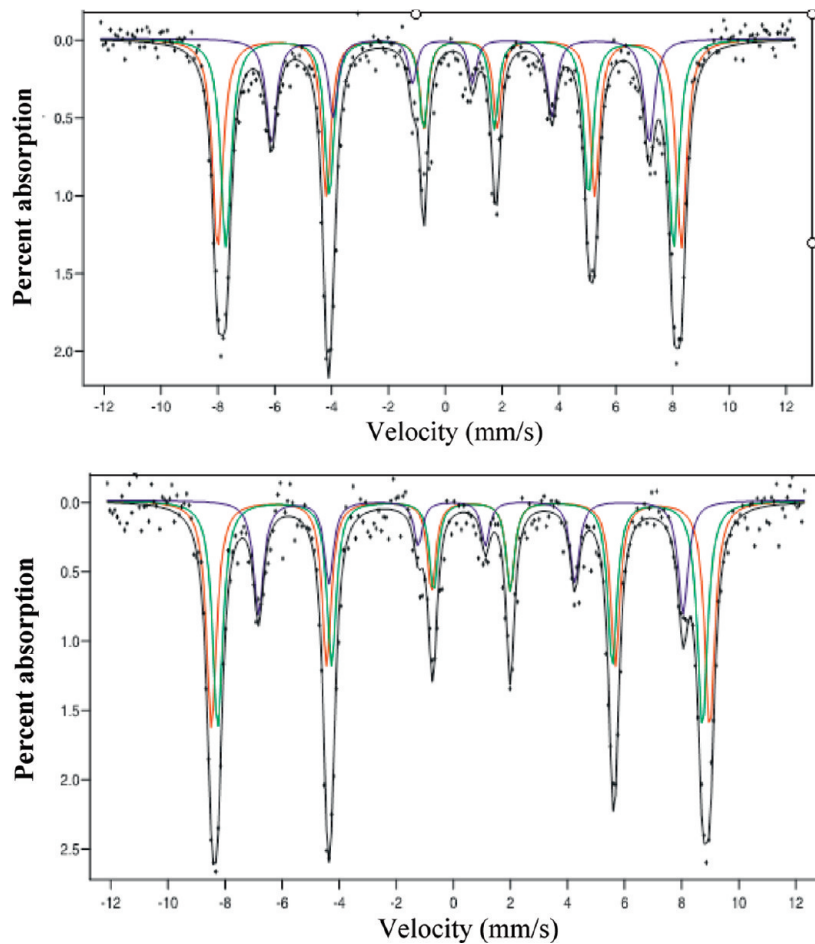


Figure 9. Mössbauer spectra of $\text{Ba}_{1.6}\text{Ca}_{2.3}\text{Y}_{1.1}\text{Fe}_5\text{O}_{13}$ at room temperature (above) and 77 K (below).

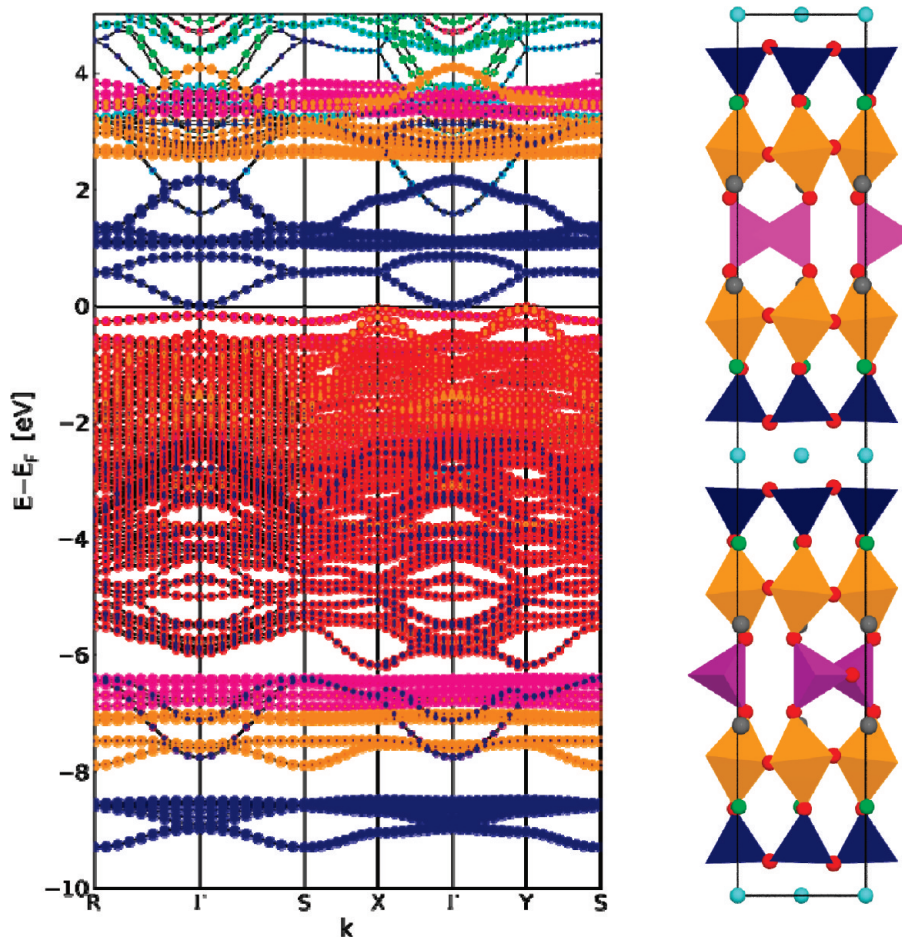


Figure 10. Electronic band structure of $\text{YBa}_2\text{Ca}_2\text{Fe}_5\text{O}_{13}$, the composition used in the DFT calculations to most closely approximate the experimentally observed composition, in the fully ordered arrangement 1, calculated using GGA+U with $U_{\text{eff}} = 5.4$ eV. Dots are added to the bands to show the projection of the states onto orbitals centered at different atoms, the radius of the dot is proportional to the extent of overlap. The dots are colored light blue for overlap onto orbitals on Y atoms, green for Ba, dark blue for Fe at square-pyramidal sites, yellow for Fe at octahedral sites, pink for Fe at tetrahedral sites, and red for O, with respective colors being retrieved on the aside structure illustration. No overlap onto orbitals at Ca atoms is seen for states in this energy range. Only states from one spin channel are shown because the band structure of both channels are the same.

nonmagnetic calculation by 4.13, 4.70, 4.60, and 5.35 eV/FU respectively. The G-type antiferromagnetic ordering is the most stable, with atomic moments on the iron atoms in the range of $3.4\text{--}3.5\ \mu_{\text{B}}$, in good agreement with experimentally determined magnetic structure.

We analyzed the electronic structure by calculating the band structure of the material, projected onto atomic-orbital-like functions centered on each atom. As the value of U_{eff} is increased from 4.3 to 5.4 eV, an indirect band gap opens up, but remains small at 0.02 eV for $U_{\text{eff}} = 5.4$ eV. The band structure calculated with $U_{\text{eff}} = 5.4$ eV (Figure 10), can be compared to those calculated with the GGA functional, and with $U_{\text{eff}} = 4.3$ eV (see Figure S15 in the Supporting Information).

For all functionals, the electronic structure around the band gap is dominated by states with O 2p and Fe 3d character. In the GGA+U calculations, the electronic bands below the band gap, down to an energy of about 6 eV, have largely O 2p character, with some admixture of Fe 3d states from different sites. At lower energies, and above the band gap to an energy of about 4 eV, the bands have predominately Fe 3d character. The contributions from the different Fe sites are split in energy, with the

states from the five coordinated square pyramidal sites lowest in energy, and then states localized at the six coordinated octahedral and four coordinated tetrahedral sites with increasing energies.

Interestingly, analysis of the projected band structure shows that the gap is between states localized in different areas of the structure. The top of the valence band consists of hybridized O 2p and Fe 3d states centered on the iron tetrahedral sites, whereas the bottom of the conduction band consists of O 2p and Fe 3d_{z²} states centered at the square pyramidal sites. The nature of these bands can be seen in more detail in the electron density plots (Figure 11).

Calculations with G-type antiferromagnetic ordering were also performed for arrangement 3, which was the second most stable structure with nonspin polarized calculations and is the closest to the experimentally determined site occupancies. With spin-polarized GGA calculations, this arrangement was still found to be less stable than the fully ordered system, but only by 0.05 eV/FU. In contrast, inclusion of the onsite Coulomb term caused it to become more stable than the fully ordered system by 0.22 eV with $U_{\text{eff}} = 4.3$ and 0.26 eV/FU with $U_{\text{eff}} = 5.4$ eV. It would seem that a more correct treatment of the correlation

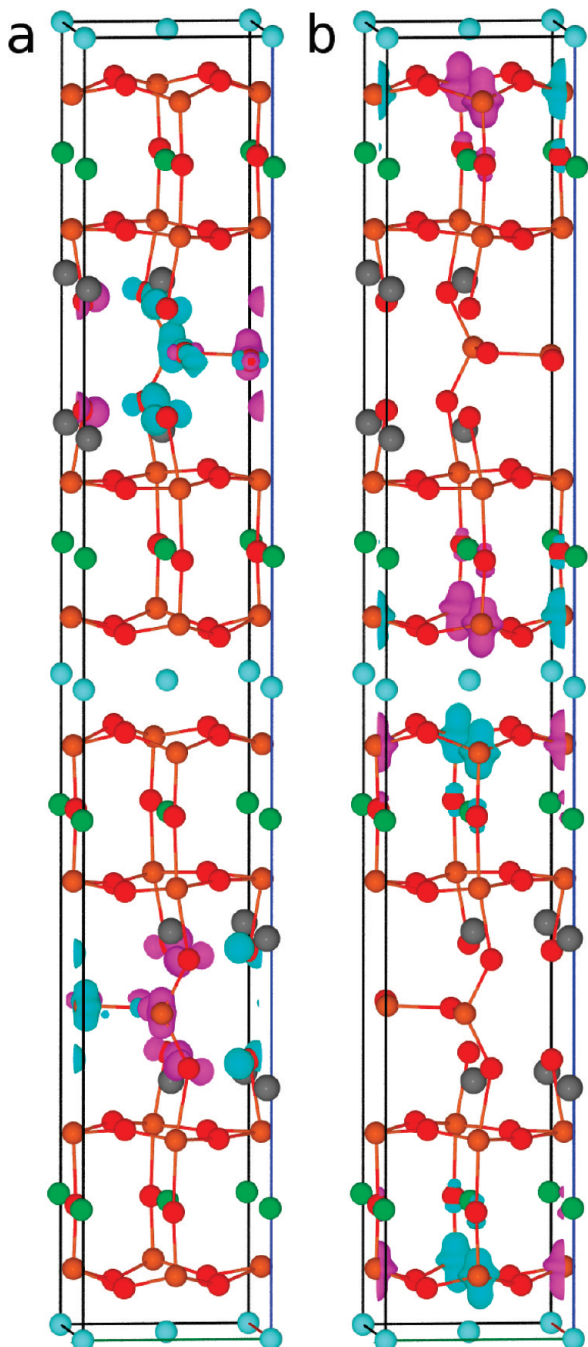


Figure 11. Electron density of the state at (a) the top of the valence band and (b) at the bottom of the conduction band calculated with GGA+U with $U_{\text{eff}} = 5.4$ eV and the fully ordered arrangement 1. Spin densities from the two different spin channels are shown in light blue and pink. Atoms are colored light blue for Y, green for Ba, gray for Ca, orange for Fe, and red for O. Densities are shown at contours of $0.034 \text{ e}^- \text{ \AA}^{-3}$.

energy is necessary to correctly predict the mixed composition of the A sites in this structure.

The partial density of states is calculated by projecting onto orbitals centered at the atomic positions within the structure (Figure 12). Unlike with the fully ordered A sites, a band gap is present even without the inclusion of the onsite Coulomb correction, and widens from 0.28 eV in the GGA calculation to 1.87 eV with $U_{\text{eff}} = 4.3$ eV, and 2.01 eV with $U_{\text{eff}} = 5.4$ eV. Comparison of the electronic structures of arrangement 3 and the fully

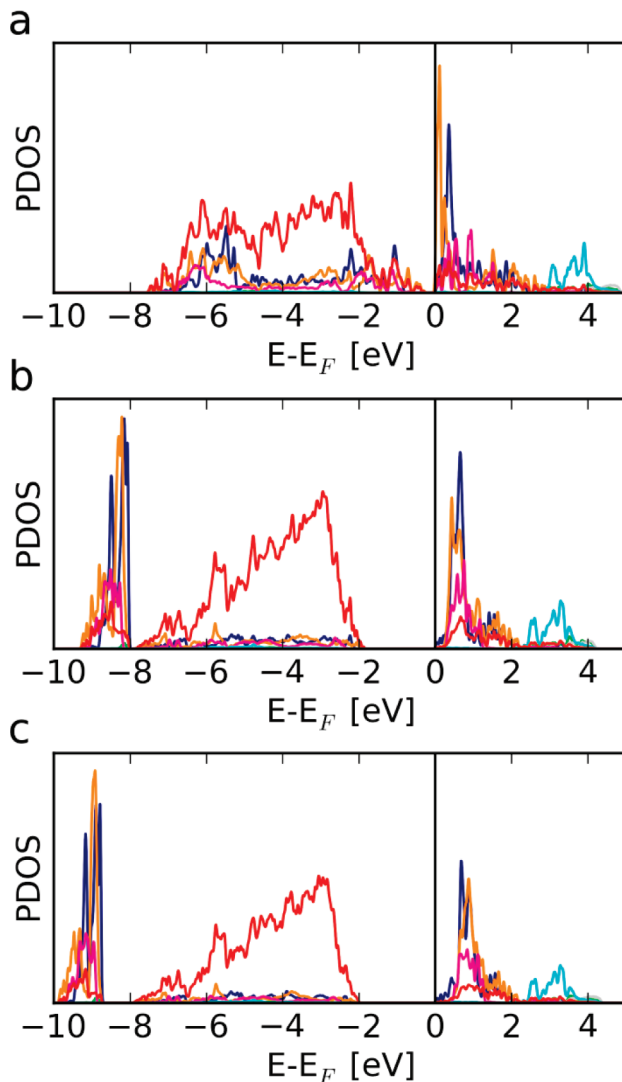


Figure 12. Partial density of states calculated using (a) GGA, (b) GGA+U, $U_{\text{eff}} = 4.3$ eV and (c) GGA+U, $U_{\text{eff}} = 5.4$ eV for arrangement 3 of $\text{YBa}_2\text{Ca}_2\text{Fe}_5\text{O}_{13}$. The density of states is projected onto atomic orbitals centered at the positions of the atoms. The different colors represent overlap onto different atoms, using the same color scheme as in Figure 10.

ordered arrangement 1 suggests that the opening of a band gap is mainly due to the change in energy of the unoccupied Fe 3d orbitals at the square-pyramid sites. This is due to the change in the electrostatic potential at the square-pyramid site caused by the incorporation of Ca^{2+} ions in the neighboring Y^{3+} layer (Figure 13).

In the case of arrangement 1, the potential at the square-pyramid sites is more negative than at either of the two B sites. This is presumably due to the proximity of triply charged Y^{3+} ions in the neighboring A sites, rather than the doubly charged Ba^{2+} and Ca^{2+} ions. As a result, Fe 3d states localized at the square pyramid sites are lower in energy than ones in the octahedral and tetrahedral sites. This effect is also observed for $\text{YBa}_2\text{Fe}_3\text{O}_8$.⁴⁴ Following mixing of the Y^{3+} and Ca^{2+} ions in arrangement 3, the potential at the square-pyramid Fe center is less negative than in the fully ordered structure and hence the states localized at the

(44) Xu, Y.; Hao, X.; Lü, M.; Wu, Z.; Zhou, D.; Meng, J. *Solid State Commun.* **2008**, 147, 130–133.

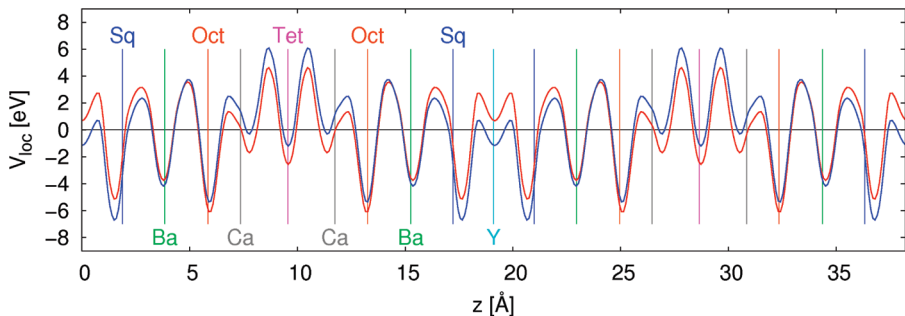


Figure 13. Calculated local electrostatic potential for $\text{YBa}_2\text{Ca}_2\text{Fe}_5\text{O}_{13}$ for the fully ordered arrangement 1 (blue) and arrangement 3 (red). The potential has been averaged over the ac plane to show the variation in the direction of the long axis. The positions of the atoms along this axis are indicated by vertical colored lines, with the same color scheme as in Figure 10.

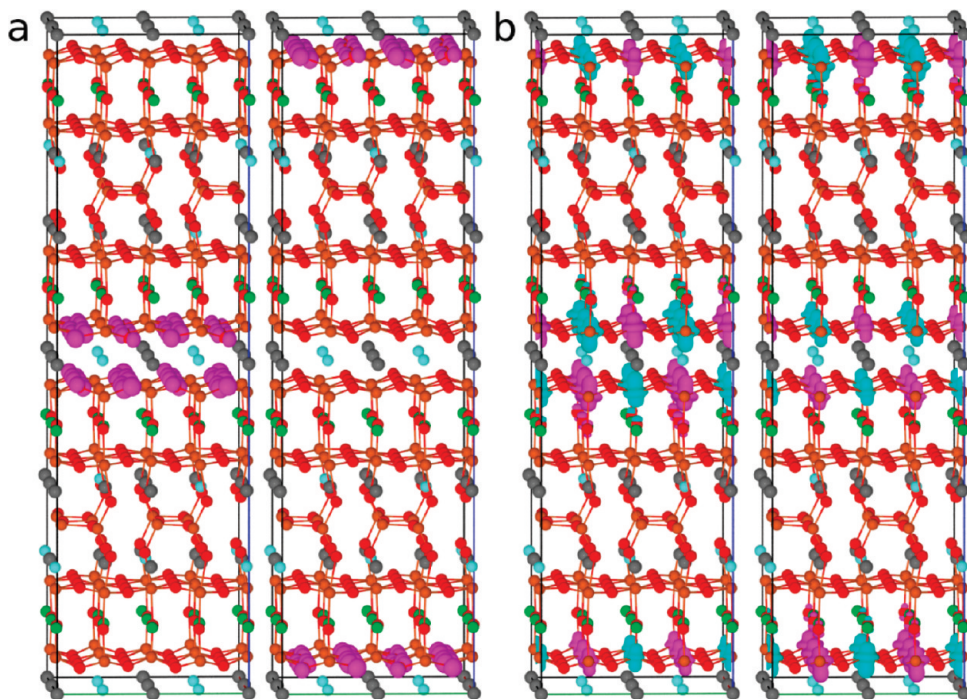


Figure 14. Electron density of the two doubly degenerate states at (a) the top of the valence band and (b) at the bottom of the conduction band calculated with GGA+U with $U_{\text{eff}} = 5.4$ eV and arrangement 3 of the A site cations, which most closely matches the experimental observations. In b, the spin density from the two different spin channels are shown in light blue and pink. As the two spin densities were identical in a, only one is shown. Atoms are colored as in Figure 10 and densities are shown at contours of $0.007 \text{ e}^- \text{ Å}^{-3}$.

square-pyramid sites increase in energy, becoming roughly the same as states at the other two B sites. In the case of the unoccupied orbitals at the square pyramid sites, which form the conduction band edge, this results in the opening of a significant band gap.

In addition, the nature of the sites at the valence band edge and conduction band edge are different when the Ca and Y layers are mixed. The electron density arising from the top two states of the valence band and the bottom two of the conduction band are shown (Figure 14). The valence band edge are O 2p orbitals at the base of the square-pyramids, whereas the conduction band edge is formed from Fe 3d_{z²} orbitals at the square-pyramid sites. The band gap transition is now between states which are all localized near the square-pyramid sites.

The increased localization of the Fe 3d states in the GGA+U method will tend to emphasize the effects caused by the change in the local electrostatic potential at

the B sites. This may be the reason why the GGA+U method is required to correctly predict that the mixing of Y^{3+} ions and Ca^{2+} ions in arrangement 3 gives a more stable structure than the fully ordered arrangement 1.

The band structure in Figure 10 only shows dispersion along the shorter real-space axes. Dispersion in the long axis direction is very small in comparison (see Figure SI6 in the Supporting Information), less than 0.1 eV across the Brillouin zone for states near the band gap. This suggests that the electronic structure in the material is largely 2D in character, a fact supported by the localization in the long-axis direction of the states at the edges of the band gap shown in Figures 11 and 14. We have also calculated the electronic band structure of $\text{YBa}_2\text{Fe}_3\text{O}_8$ using the same settings and a U_{eff} of 5.4 eV (see Figure SI7 in the Supporting Information). Most of the states in $\text{YBa}_2\text{Fe}_3\text{O}_8$ also lack significant dispersion in the direction of the long axis. This is consistent with the hypothesis

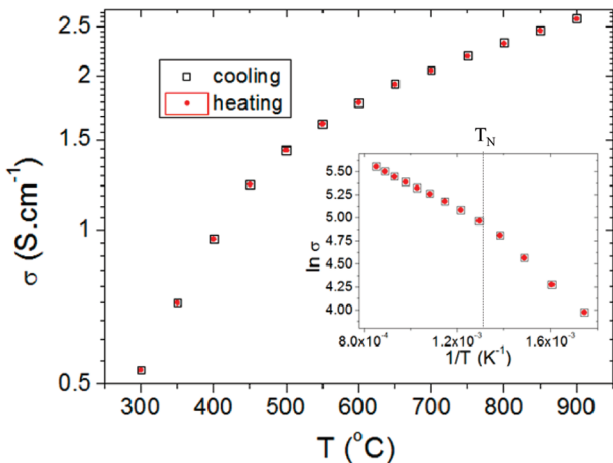


Figure 15. DC conductivity of $\text{Ba}_{1.6}\text{Ca}_{2.3}\text{Y}_{1.1}\text{Fe}_5\text{O}_{13}$, collected upon heating and cooling. Dashed line on the inserted $\ln \sigma = f(1/T)$ curve marks the Neel transition temperature.

that the O vacancies in the layer with eight-coordinate A sites reduce electronic interactions across this layer in these structures. In the structure of $\text{Ba}_{1.6}\text{Ca}_{2.3}\text{Y}_{1.1}\text{Fe}_5\text{O}_{13}$ the Fe ions either side of this layer are separated by 3.77 Å, without any bridging O atoms. Electronic overlap between these Fe atoms is therefore presumably small, leading to a pseudo-2D band structure.

Physical Characterization. The material's transport properties were investigated as a function of temperature. A semiconducting behavior is observed over the temperature range 300–900 °C, with values of conductivity increasing from 0.53 to 2.59 S cm^{-1} (Figure 15). These values denote the lack of charge carriers in the compound, for which electronic and magnetic properties are governed by the predominance of Fe^{3+} . In addition, the largely 2D electronic structure calculated using DFT, may contribute to the material's relatively low electronic conductivity in a pellet containing randomly oriented grains. A change of slope is observed in the $\ln \sigma$ vs $1/T$ curve at ~ 480 °C, which can be correlated with the magnetic transition temperature T_N . This effect was reported in the $\text{Nd}_{1-x}\text{Ca}_x\text{FeO}_{3-y}$ system⁴⁵ and attributed to a variation of electrical activation energy after the change in spin alignment. The activation energies were calculated to be 200 and 111 meV, respectively below and above the T_N of the material, comparing well with Fe^{3+} parent systems $\text{YBa}_2\text{Fe}_3\text{O}_8$ and $\text{Ca}_2\text{Fe}_2\text{O}_5$ (respectively 420 and 280 meV).^{46,47} The conductivity of the sample also shows total reversibility upon a cycle of cooling and heating, which is consistent with the high stability of the sample and the fixed oxygen content over the studied temperature range.

AC impedance spectroscopy was performed on a symmetrical cell with Sm-doped ceria as the electrolyte, to evaluate the electrochemical activity of this phase toward

the oxygen reduction reaction (ORR) (Figure 16), after checking both materials showed no reaction together (see Figure SI8 in the Supporting Information). At 700 °C and below, the AC impedance arcs were modeled by an equivalent circuit composed of an ohmic resistance (representing the resistance associated with the electrolyte and the cables), in series with two resistors, each in parallel with a constant phase element (CPE), representing the electrode processes of mass transport and charge transfer. Above 700 °C, the impedance arcs could be modeled by an ohmic resistance in series with a single resistor-CPE in parallel, indicating that at these temperatures the cathode rate limiting step is dominated by a single process. The DC conductivity measurements indicate that the electrical conductivity of the 10-layer material is several orders of magnitude lower than that of common SOFC cathode materials, with a value of 2.06 S cm^{-1} at 700 °C, compared with 320 S cm^{-1} for the widely used iron-rich cathode $\text{La}_{0.6}\text{Sr}_{0.4}\text{Fe}_{0.8}\text{Co}_{0.2}\text{O}_{3-\delta}$ at the same temperature.⁴⁸ This suggests that the cathode performance (ASR) is likely to be limited by low electronic conductivity correlated with the lack of charge carriers in this material. However, the value of the area specific resistance of 0.87 $\Omega \text{ cm}^2$ at 700 °C (Figure 16), compares with the cobalt-free $\text{Ba}_{0.5}\text{Sr}_{0.5}\text{Fe}_{0.8}\text{Zn}_{0.2}\text{O}_{3-\delta}$ (0.22 $\Omega \text{ cm}^2$ at 700 °C) or the widely used iron-rich cathode $\text{La}_{0.6}\text{Sr}_{0.4}\text{Fe}_{0.8}\text{Co}_{0.2}\text{O}_{3-\delta}$ (0.44 $\Omega \text{ cm}^2$ at 690 °C on Gd-doped ceria) while remaining 1 order of magnitude higher than the best values obtained for cobalt compounds like $\text{SmBa}_{0.5}\text{Sr}_{0.5}\text{Co}_2\text{O}_{5+\delta}$ (0.019 $\Omega \cdot \text{cm}^2$ at 700 °C on Gd-doped ceria). If one supposes the rate limiting process of this low conducting material to be charge transfer, whereby the adsorbed oxygen species combine with electronic charge carriers to form O^{2-} ions, then the relatively low ASR indicates an enhanced activity for the contributions related to the mass transport processes of oxygen adsorption and incorporation as well as oxygen ion diffusion in the bulk, to balance the overall behavior. In that sense, the 10-layered ordered structure could be directly responsible for these phenomena, with fully oxygen deficient layers favoring atomic diffusion. Indeed, with the presence of FeO_5 square-based pyramid layers, this material has common structural features to one of the most promising class of mixed conductors, the $\text{LnBaCo}_2\text{O}_{5+x}$ (112 layered perovskites, Ln = lanthanide) materials, showing excellent activity toward the ORR process. Furthermore the complex atomic ordering might induce the presence of specific transition metal polyhedra on the cathode surface which, as suggested by Huang and Goodenough⁴⁹ could improve catalytic activity, in comparison to a simple perovskite material. Emphasizing that point is the lower activation energy for the ORR process with this ten layered $\text{Ba}_{1.6}\text{Ca}_{2.3}\text{Y}_{1.1}\text{Fe}_5\text{O}_{13}$, $E_a = 1.43$ eV, than for cubic phases such as $\text{La}_{0.8}\text{Sr}_{0.2}\text{CoO}_{3-\delta}$ ($E_a = 1.70$ eV), $\text{La}_{0.8}\text{Sr}_{0.2}\text{FeO}_{3-\delta}$ ($E_a = 1.90$ eV), or $\text{La}_{0.8}\text{Sr}_{0.2}\text{Co}_{0.8}\text{Fe}_{0.2}\text{O}_{3-\delta}$ ($E_a = 2.09$ eV).

(45) Yo, C. H.; Jung, I. Y.; Ryu, K. H.; Ryu, K. S.; Choy, J. H. *J. Solid State Chem.* **1995**, *114*, 265–270.

(46) Matsumoto, Y.; Hombo, J. *J. Solid State Chem.* **1991**, *93*, 395–402.

(47) Shaula, A. L.; Pivak, Y. V.; Waerenborgh, J. C.; Gaczyński, P.; Yaremchenko, A. A.; Kharton, V. V. *Solid State Ionics* **2006**, *177*, 2923–2930.

(48) Tai, L. W.; Nasrallah, M. M.; Anderson, H. U.; Sparlin, D. M.; Sehlin, S. R. *Solid State Ionics* **1995**, *76*, 273–283.

(49) Huang, K.; Goodenough, J. B., *Solid Oxide Fuel Cell Technology*; Woodhead Publishing: Cambridge, U.K., 2010, pp 35–38.

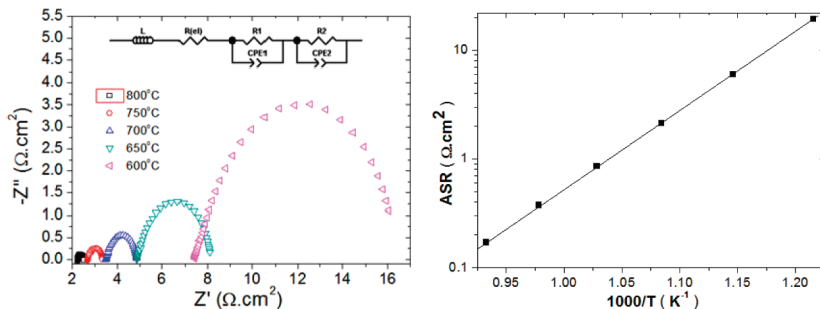


Figure 16. AC impedance spectroscopy and ASR plot for the symmetrical cell $\text{Ba}_{1.6}\text{Ca}_{2.3}\text{Y}_{1.1}\text{Fe}_5\text{O}_{13}/\text{SDC}/\text{Ba}_{1.6}\text{Ca}_{2.3}\text{Y}_{1.1}\text{Fe}_5\text{O}_{13}$.

From the structural point view, if one considers the presence of the transition metal in a square-based pyramidal environment as a critical point for rapid O_2 molecule dissociation, this structure can be seen as a diluted version of 112 layered perovskites, because along the stacking axis only 2/5 of Fe containing layers display these features, whereas all of the layers would display five coordinated transition metals in the 112 type. Hence, this could be regarded as a reason why lower activation energies (≈ 1.2 eV) can be found in $\text{LnBaCo}_2\text{O}_{5+x}$ (Ln = lanthanide). However, the proportions of square-based pyramids per formula unit are similar in both compounds, as a result of a large oxygen nonstoichiometry in the 112 type, which is not present in $\text{Ba}_{1.6}\text{Ca}_{2.3}\text{Y}_{1.1}\text{Fe}_5\text{O}_{13}$ material, because of a fully oxygen-deficient layer that makes the concerned iron site totally available for oxygen molecule attack. The lower activation energies observed in $\text{LnBaCo}_2\text{O}_{5+x}$ can as well be seen as the result of a higher charge-transfer contribution, because of electronic conductivities two orders magnitude higher than in the present compound, assigned to the 112 materials being cobalt- rather than iron-based.

It should also be noted that our ASR values were obtained without any optimization of the cathode microstructure, and a relatively high cell firing temperature of 1150 °C. It is well-known that improving the cathode microstructure⁵⁰ and reducing the cell firing temperature⁵¹ can lead to a significant reduction in ASR values, suggesting further improvements in the ASRs can be made.

Discussion

$\text{Ba}_{1.6}\text{Ca}_{2.3}\text{Y}_{1.1}\text{Fe}_5\text{O}_{13}$ is isostructural with $\text{Ba}_2\text{Ca}_2\text{Nd}_2\text{Fe}_6\text{O}_{15.6}$ and can be described as a regular intergrowth between $\text{Ca}_2\text{Fe}_2\text{O}_5$ and $\text{YBa}_2\text{Fe}_3\text{O}_8$, leading to a complex superstructure displaying 20 times the unit-cell volume of a classic cubic perovskite. However, the distinct compositions and preferences of the trivalent A site cation lead to considerable changes in the A site ordering. Indeed, $\text{Ba}_{1.6}\text{Ca}_{2.3}\text{Y}_{1.1}\text{Fe}_5\text{O}_{13}$ shows a degree of order superior to $\text{Ba}_2\text{Ca}_2\text{Nd}_2\text{Fe}_6\text{O}_{15.6}$ when compared to the ideal $(\text{Y}, \text{Nd})\text{-Ba}_2\text{Ca}_2\text{Fe}_5\text{O}_{13}$ intergrowth, where the eight-coordinate site would be Y^{3+} (Nd^{3+}), the nine-coordinated Ca^{2+} and the 12-coordinated Ba^{2+} . This perfect ordering is not reached

in either of the two compounds, but is clearly stronger in $\text{Ba}_{1.6}\text{Ca}_{2.3}\text{Y}_{1.1}\text{Fe}_5\text{O}_{13}$, which can be described as well-ordered, with 66% Y^{3+} , 80% Ca^{2+} , and 90% Ba^{2+} on the sites that should be fully occupied by each of these cations in an ideal intergrowth. One can also consider that it may be difficult to avoid $\text{Y}^{3+}\text{-Ca}^{2+}$ site disorder, because of their close ionic radii, which should provoke deviations from the ideal ordering. Results from DFT calculations also confirm this tendency, by showing that compounds with mixed Ca/Y sites will be energetically favored compared to related ones with mixed Ba/Ca sites, even without Ba-Ca non-stoichiometry. Taking these considerations into account, one should note the eight and nine coordinated sites are almost exclusively filled with the smaller Y^{3+} and Ca^{2+} cations, at 100 and 95%, respectively, whereas the larger Ba^{2+} is still 90% of the 12 coordinated A site. In $\text{Ba}_2\text{Ca}_2\text{Nd}_2\text{Fe}_6\text{O}_{15.6}$, the comparable occupancy numbers are 75% Nd^{3+} , 43% Ca^{2+} , 40% Ba^{2+} in the expected sites, which clearly shows that the ordering in nine and 12 coordinated sites is not as well achieved, although a preferential ordering is still observed. This has to be also seen as a result of a composition which slightly deviates from the ideal $\text{LnBa}_2\text{Ca}_2\text{Fe}_5\text{O}_{13}$ (Ln = lanthanide or Y), added to the fact that Nd^{3+} has a greater ionic radius than Y^{3+} , which might favor the possibility of Ba/Nd mixed layers more easily.

Moreover, strong differences are also observed in the chemical behavior of the two ten layer structures. $\text{Ba}_2\text{Ca}_2\text{Nd}_2\text{Fe}_6\text{O}_{15.6}$ was obtained only after several heating cycles in various atmospheres, with a final highly reducing treatment in the presence of a Zr getter affording an air sensitive material, most probably because of the low Fe oxidation state of +2.66. In contrast, a careful selection of the cation composition allows $\text{Ba}_{1.6}\text{Ca}_{2.3}\text{Y}_{1.1}\text{Fe}_5\text{O}_{13}$ to be stabilized under ambient conditions, with a considerably easier synthetic process. Several characterization techniques are in agreement with the Fe^{3+} oxidation state in this compound, which leads to the difference in respective stabilities of the two ten layer perovskites.

Indeed, the structure shows a clear robustness upon heating, as shown by the X-ray thermodiffraction measurements. $\text{Ba}_{1.6}\text{Ca}_{2.3}\text{Y}_{1.1}\text{Fe}_5\text{O}_{13}$ shows that the ten layer structure can not only be accessed under more oxidizing conditions than the original highly reduced example, but can also be stable over a wide temperature range. Along with the Fe^{3+} oxidation state that is well-suited to ambient atmosphere stability, the cation ordering, that goes with

(50) Haanappel, V. A. C.; Mertens, J.; Rutenbeck, D.; Tropartz, C.; Herzhof, W.; Sebold, D.; Tietz, F. *J. Power Sources* **2005**, *141*, 216–226.

(51) Tarancón, A.; Skinner, S. J.; Chater, R. J.; Hernandez-Ramirez, F. *J. Mater. Chem.* **2007**, *17*, 3175–3181.

preferential coordination numbers for each A site imposes a specific oxygen sublattice along the stacking sequence. This “cation-imposed” oxygen ordering might be a reason why the superstructure is retained even at high temperature, whereas in the less-ordered (at the A site level) reduced $\text{Ba}_2\text{Ca}_2\text{Nd}_2\text{Fe}_6\text{O}_{15.6}$, the oxygen sublattice undergoes an order–disorder transition starting as low as 500 °C.

In the present case, the electronic and magnetic properties of the material are governed by the Fe^{3+} charge state; in particular, the low d.c. conductivity can be attributed to the Mott–Hubbard gap produced by interelectron repulsion. The observed experimental conductivity can be assigned to defects arising from the deviation from a pure Fe^{3+} composition, as the observed gaps, considerably smaller than the predicted intrinsic DFT gap, are consistent with extrinsic transport due to states within the Mott–Hubbard gap. DFT calculations suggest a strong influence of the A site order on the electronic properties of the material. The composition at the different A site positions affects the electrostatic potential at the neighboring B sites. In the case of $\text{Ba}_{1.6}\text{Ca}_{2.3}\text{Y}_{1.1}\text{Fe}_5\text{O}_{13}$ fractional occupation of the triply charged Y^{3+} cations and doubly charged Ca^{2+} and Ba^{2+} cations at the different A sites alters the relative energies of the Fe d-orbitals at the different B sites. The addition of Ca^{2+} into the Y^{3+} layer and of Y^{3+} into the Ca^{2+} layer of the fully ordered arrangement 1 to give arrangement 3, a distribution of cations closer to the experimentally determined distribution, causes a significant increase in the calculated electronic band gap, alters the nature of the states at the top of the valence band and increases the stability of the material. The extent of A site disorder has a large effect on the nature and energy of the frontier electronic states at the top of the valence band and bottom of the conduction band. Not only are these states important in terms of the electronic conductivity of a material, they are also important in determining the catalytic activity, both necessary functional properties for applications as a solid oxide fuel cell cathode. The strong dependence of the material’s stability and electronic and catalytic properties on A site order illustrates well the possibilities opened up by the complex crystal chemistry in this type of compound.

This material has some advantages for high-temperature applications, due to both its thermal stability and lack of reactivity both to common electrolytes and to CO_2 . The observed ASR is significantly lower than would be expected based on the poor d.c. conductivity, which suggests that the combined oxide ion transport and oxygen reduction catalysis performance of this material is good, warranting further investigation into the cathode performance of materials with related structures. Good ionic conductivity can be explained by the presence within the structure of the oxygen-free rock salt layers found in some of the most promising solid oxide fuel cell cathodes such as the 112 perovskites $\text{LnBaCo}_2\text{O}_{5+\delta}$ (Ln = lanthanide or Y).^{8,52} Because it has been proposed that square-

based pyramids are favorable environments for transition metals to catalyze dioxygen molecule dissociation, while tetrahedral Fe^{3+} will be shielded from O_2 attack,⁴⁹ and given that the specific A site ordering might also form these polyhedra at the surface of the material, the 112-type layers in the ten-layered material could also be important for catalytic behavior. The calculations show that both the lowest energy levels in the conduction band and the highest in the valence band are associated with these square-based pyramidal Fe sites, which may enhance the role of any of these sites present at the surface in the adsorption of oxygen molecules and subsequent dissociation. Once this process has occurred, oxide anions can easily diffuse through the fully oxygen deficient layer available at the same level of the crystal structure. Such considerations may contribute to the low activation energy found for the ORR process in $\text{Ba}_{1.6}\text{Ca}_{2.3}\text{Y}_{1.1}\text{Fe}_5\text{O}_{13}$, compared to simpler cubic perovskites. It is also interesting to note that the electronic structure of $\text{YBa}_2\text{Fe}_3\text{O}_8$ is similar, with states at the square based pyramidal Fe site at the bottom of the conduction band. Therefore, a more general outcome of such calculations is that these types of layered structures, combining low energy levels in the conduction band with square-based pyramidal sites for transition metals and that may directly incorporate dissociated species in the neighboring fast anion conducting layer, are promising candidates for the discovery of new materials showing high efficiency for the ORR process.

Regarding the SOFC stability, the volumetric thermal expansion coefficient ($\alpha_v = 35.4 \times 10^{-6} \text{ K}^{-1}$) of $\text{Ba}_{1.6}\text{Ca}_{2.3}\text{Y}_{1.1}\text{Fe}_5\text{O}_{13}$ is strikingly similar to the SDC electrolyte ($\alpha_v = 37.5 \times 10^{-6} \text{ K}^{-1}$), when compared to $\alpha_v = 49.2 \times 10^{-6} \text{ K}^{-1}$ in $\text{GdBaCo}_2\text{O}_{5+\delta}$, or $57.6\text{--}68.7 \times 10^{-6} \text{ K}^{-1}$ of the simple cubic perovskite $\text{Ba}_{0.5}\text{Sr}_{0.5}\text{Co}_{0.8}\text{Fe}_{0.2}\text{O}_{3-\delta}$ (values extrapolated from linear thermal expansion coefficients given in^{53,54}). Additionally, as a complementary test of the compound stability, the sample was annealed at 700 °C for 24 h under pure CO_2 . Although this treatment is known to result into total phase decomposition for some related Ba-containing perovskites such as $\text{GdBaCo}_2\text{O}_{5+\delta}$, with the formation of BaCO_3 ,²⁵ the sample remains unchanged after this annealing and no trace of BaCO_3 could be observed. The material can still be considered as rich in Barium, which is approximately 1/3 of the total A site composition. Moreover, a system like $\text{Ba}_{1-x}\text{Sr}_x\text{Co}_{0.8}\text{Fe}_{0.2}\text{O}_{3-\delta}$ shows carbonate formation for the well-known $x = 0.5$ compound,²⁶ but also for values as high as $x = 0.8$, where Ba represents only 1/5 of the A site composition,²⁷ emphasizing the robustness of the present ten layer compound. Therefore, this new mixed conductor matches well to several SOFC cathode requirements, and provided that there are ways to improve electrical conductivity in Fe^{3+} systems by doping to control the band filling, its structure represents an opportunity to generate new relevant materials in this area.

(52) McKinlay, A.; Connor, P.; Irvine, J. T. S.; Zhou, W. *J. Phys. Chem.* **2007**, *111*, 19120.

(53) Tarancón, A.; Marrero-López, D.; Peña-Martínez, J.; Ruiz-Morales, J. C.; Núñez, P. *Solid State Ionics* **2008**, *179*, 611–618.

(54) Zhu, Q.; Jin, T.; Wang, Y. *Solid State Ionics* **2006**, *177*, 1199–1204.

Acknowledgment. A.D. and M.D. are supported by the European Research Council (ERC Grant agreement 227987). R.S. and H.N. are supported by EPSRC (EP/H000925), and M.T. by a Doctoral Training Award from EPSRC. Via our membership of the UK's HPC Materials Chemistry Consortium, which is funded by EPSRC (EP/F067496), this work made use of the facilities of HECToR, the UK's national high-performance computing service,

which is provided by UoE HPCx Ltd. at the University of Edinburgh, Cray Inc. and NAG Ltd., and funded by the Office of Science and Technology through EPSRC's High End Computing Programme.

Supporting Information Available: Additional figures and tables (PDF). This material is available free of charge via the Internet at <http://pubs.acs.org>.